

# A new soil-based approach for empirical monitoring of enhanced rock weathering rates

Tom Reershemius<sup>1\*</sup> and Mike E. Kelland<sup>2\*</sup>, Jacob S. Jordan<sup>3</sup>, Isabelle R. Davis<sup>1,4</sup>, Rocco D'Ascanio<sup>1</sup>, Borianna Kalderon-Asael<sup>1</sup>, Dan Asael<sup>1</sup>, Dimitar Z. Epihov<sup>2</sup>, David J. Beerling<sup>2</sup>, Christopher T. Reinhard<sup>5</sup>, Noah J. Planavsky<sup>1</sup>

<sup>1</sup>Department of Earth and Planetary Sciences, Yale University, New Haven, CT, USA

<sup>2</sup>Leverhulme Centre for Climate Change Mitigation, School of Biosciences, University of Sheffield, Sheffield, UK

<sup>3</sup>Porecast Research, Lawrence, KS, USA

<sup>4</sup>School of Ocean and Earth Science, University of Southampton Waterfront Campus, Southampton, UK

<sup>5</sup>School of Earth and Atmospheric Sciences, Georgia Institute of Technology, GA, USA

\*corresponding and equal contribution authors: [tom.reershemius@yale.edu](mailto:tom.reershemius@yale.edu), [mekelland1@sheffield.ac.uk](mailto:mekelland1@sheffield.ac.uk).

Preprint: <https://doi.org/10.48550/arXiv.2302.05004>

**Significance statement:** Greenhouse gas management through Carbon Dioxide Removal (CDR) is essential for augmenting mitigation of CO<sub>2</sub> emissions to limit future climate change. Enhanced Rock Weathering (ERW) is a form of CDR involving the amendment of soils with crushed silicate rock, with the potential to permanently remove billions of tons of carbon dioxide from the atmosphere. However, effective implementation of this approach requires robust Monitoring, Reporting and Verification (MRV) of CO<sub>2</sub> removal by rock grain weathering. We describe and empirically validate a geochemical mass-balance approach for tracking rates of ERW in soils and the corresponding carbon capture. The soil sampling requirements for this approach integrate with existing agronomic practices, demonstrating the potential for implementation at scale.

**Abstract:** Enhanced Rock Weathering (ERW) is a promising scalable and cost-effective Carbon Dioxide Removal (CDR) strategy with significant environmental and agronomic co-benefits. However, a major barrier to the widescale implementation of ERW is a robust Monitoring, Reporting, and Verification (MRV) framework. To successfully quantify the amount of carbon dioxide removed by ERW at scale, MRV must be accurate, precise, and cost-effective. Here, we outline a new method based on mass balance where metal analysis on soil samples is used to accurately track the extent of *in-situ* alkaline mineral weathering. We show that signal-to-noise issues of *in-situ* soil analysis can be mitigated by using isotope-dilution mass spectrometry to reduce analytical error. We implement a proof of concept experiment demonstrating the method in controlled mesocosms. In our experiment, basalt feedstock is added to soil columns containing the cereal crop *Sorghum bicolor* at a rate equivalent to 50 t ha<sup>-1</sup>. Using our approach, we calculate an average initial CDR value of 2.24 ± 1.33 tCO<sub>2</sub>eq ha<sup>-1</sup> from our experiments after 235 days, within error of an independent estimate calculated using conventional elemental budgeting of reaction products. Our result corresponds to an initial CDR efficiency of 24.4 ± 14.5 % for the feedstock used. Our method provides a robust time-integrated estimate of initial CDR, and offers a path to track and validate large-scale carbon removal through ERW.

## 1 Introduction

Avoiding 2°C of global warming by 2100 will require significant carbon emissions reduction. Governments must implement policy with increasingly stringent year-on-year carbon mitigation targets (1, 2). Despite recent progress, the implementation of all current policies will result in a 12 gigatonne ( $10^9$  tonnes) CO<sub>2</sub>-equivalent shortfall to climate goals as outlined by the Paris Agreement (3). In the absence of feasible pathways to sufficiently reduce carbon emissions, large-scale Carbon Dioxide Removal (CDR) is essential for augmenting decarbonization efforts in the coming century (e.g., 4, 5).

Enhanced Rock Weathering (ERW) is a promising CDR technique where naturally occurring mineral weathering reactions that consume atmospheric CO<sub>2</sub> are accelerated. Typically, this may be achieved by applying crushed silicate rocks with a high reactive surface area to agricultural and forest soils (e.g., 6-20). Potential advantages and co-benefits of ERW include: a low technological barrier to implementation at scale (8, 13); long-term storage of carbon compared to organic reservoirs (>10,000 years) (21-27); supply of key nutrients for crop growth (13, 28-33). Additionally, ERW feedstocks such as basalt may be used for the deacidification of soils, filling the role of agricultural lime (currently a net source of CO<sub>2</sub> to the atmosphere; 34-42). Several recent studies have improved our understanding of ERW: mechanistic modelling of weathering reactions in agricultural soils (e.g., 11, 14, 43); modelling hydrological effects on weathering rates (e.g., 44); laboratory and mesocosm experiments tracking uptake of nutrients by plants, and feedstock dissolution rates (e.g., 30, 32, 42, 45-51); and field experiments implementing ERW at scale (e.g., 52-54).

Despite these recent advances, ERW currently lacks a robust framework for Monitoring, Reporting, and Verification (MRV) of CDR rates. This represents a significant barrier to widespread implementation on voluntary or compliance markets. Varying rock weathering rates in agricultural settings with variable hydroclimatic conditions are central to uncertainties associated with carbon dioxide removal in the field (e.g., 55). Approaches to MRV that are entirely model-based are yet to be fully validated for ERW. The current generation of so-called “reactive transport models” for simulating ERW have proven useful for making testable predictions (e.g., 14, 19, 43). However, it is not yet clear whether such reactive transport models are capable of accurately predicting CDR at deployment scale. Thus, bringing ERW to industrial scale will require the incorporation of an empirical MRV framework to impart confidence to key stakeholders. The MRV framework must successfully report site- and time-specific rates of feedstock weathering while being cost-effective and minimally invasive (e.g., 56, 57).

Here we introduce a novel soil-based mass balance approach for quantitatively tracking enhanced rock weathering in soils. Our approach measures the difference in concentration of ERW feedstock *in-situ* before and after weathering. This builds on a technique that is widely used to gauge the extent and mode of weathering in natural systems (e.g., 58-70). We compare the concentrations of mineral-bound metal cations (Ca<sup>2+</sup>, Mg<sup>2+</sup>, Na<sup>+</sup>) in the solid phase of soils before and after feedstock deployment. We do this by estimating changes in the total amount of these metal cations (CAT) in a specific soil sample relative to the concentration of an immobile tracer, in this case titanium (Ti). Hereafter we refer to this method as TiCAT. As a first step towards robust validation, we compare estimates of the extent of *in-situ* basalt feedstock dissolution from TiCAT to rates determined independently from detailed pool and flux tracking (>2000 measurements) in a mesocosm experiment (see 32). We then discuss the practical advantages of this approach for industrial scale deployment of CDR through ERW, and the steps require to move from an empirical estimate of feedstock dissolution rates to robust error-bound estimates of carbon dioxide removal.

## 2 Theory

### 2.1 Solid sample mass balance approach to quantifying mineral weathering

TiCAT is a mass balance approach for estimating the time-integrated amount of basalt feedstock in a soil sample that has undergone weathering. This method builds on approaches for estimating the extent of weathering in natural systems (e.g., 58-70). Within the TiCAT framework, this involves calculating changes in the concentrations of major cations in soils that have been amended with basalt, with the assumption that basalt weathering progresses at a much faster rate than that of the background soil.

To define an unweathered parent material, we first compare soil samples after basalt amendment with soil samples representative of a pre-amendment baseline, as well as samples of the basalt feedstock. This can most readily be visualized as simple two-component mixing between a soil ( $C_s$ ) and a basalt ( $C_b$ ) endmember (**Fig. 1a**). We use the difference in concentration of an immobile trace element,  $i$  (e.g., Ti, though other elements could be used – see *Supporting Information Section 1.10*), between a post-application sample ( $C_{end}$ ) and the pre-application soil baseline, to calculate the amount of basalt that has been added to the original soil for the specific sample analyzed ( $Ti_{end} - Ti_s = Ti_{add}$ ).

Using the relative abundance of Ti and mobile major cations (CAT) in the original basalt feedstock, we can then calculate the corresponding amount of mobile major cations,  $CAT_{add}$ , from the basalt feedstock present in the soil + basalt mixture at the point of basalt application (**Fig. 1b**). For a generic cation, CAT:

$$CAT_{add} = Ti_{add} \times \frac{CAT_b - CAT_s}{Ti_b - Ti_s} + y \quad , \quad (1)$$

where  $y$  is the CAT intercept of the mixing line (**Fig. 1**). Subtracting the amount of cation in the post-application sample,  $CAT_{end}$ , and adding the soil baseline,  $CAT_s$ , we can calculate the difference in the amount of the mobile cation,  $\Delta CAT$ , between the expected amount from addition of basalt, and the observed amount in the soil + basalt mixture after weathering (**Fig. 1c**):

$$\Delta CAT = CAT_{add} + CAT_s - CAT_{end} \quad . \quad (2)$$

$\Delta CAT$  therefore represents the amount of cation loss due to basalt dissolution (i.e., exported from the solid phase) between the point of basalt application and the post-application sampling date. We can also define basalt dissolution as a fraction,  $F_D$ , where:

$$F_D = \frac{\Delta CAT}{CAT_{add}} \quad . \quad (3)$$

Multiplying  $F_D$  for each cation by the application rate of CAT in the basalt feedstock gives a value for ERW which can then be converted into an initial rate of CDR (see *Supporting Information Section 1.10* for more details).

## 2.2 Analytical requirements

Limiting analytical error is a critical aspect of the TiCAT approach — and is likely to be a critical issue for any other approach aiming to track CDR from the solid phase. This is due to the signal-to-noise ratio associated with adding feedstock to a large mass of background soil. For technically and commercially feasible feedstock application rates (likely 5-50 t ha<sup>-1</sup>, see 13), analytical error can result in overlap between error-bounded values for cation concentration of soil-feedstock mixtures before and after dissolution has occurred. In our mesocosm experiment for instance, at 5% analytical error a 75% loss of major cations from the basalt portion of a soil-feedstock mixture is resolvable only at an application rate of ~40 t ha<sup>-1</sup>, assuming the mixture is homogenized to a depth of 10cm (a common mixing regime for managed row crop systems). At 1% analytical error the same amount of cation loss is resolvable at ~5 t ha<sup>-1</sup> (**Fig. 2**). When accounting for a range of plausible dissolution and application rates analytical error must generally be limited to ~1% for our mass balance method to be accurate and widely applicable, a standard that is more stringent than that currently achievable by most commercial inorganic mass spectrometry analyses (e.g., 71, 72).

We obtain the requisite analytical precision for applying the TiCAT method using isotope dilution inductively coupled plasma mass spectrometry (ID-ICP-MS). Isotope dilution is an analytical method where the concentration of an element in a sample can be measured from the known concentration of an element in a spike solution, and the ratios of two isotopes of the same element in the natural sample and the spike respectively (e.g., 73; see also 74, 75; and see *Supporting Information Section 1.8*). Our results show that our isotope dilution technique allows for a level of measurement accuracy and precision on quadrupole ICP-MS instruments that would otherwise typically only be achievable with a magnetic sector instrument (**Fig. S6**; see also 76). Given its much lower cost and far greater availability, the ability to leverage

quadrupole ICP-MS for rapid, high-throughput analyses may ultimately be a critical factor in making this MRV technique economically viable at scale.

### 3 Validation through mesocosm ERW experiments

As an initial test of the TiCAT method we employed mesocosm ERW experiments, which allow us to independently estimate ERW and CDR by measuring the concentration of reaction products in plant, soil exchangeable fraction and leachate solution pools (see 28, 30, 32, 45-49, 51, 54). Each mesocosm contained a single C4 cereal crop *Sorghum bicolor* plant (see 32) with two different fertilizer treatments (nitrogen-phosphorus-potassium, NPK, or manure), to which a basalt feedstock was added equivalent to an application rate of  $5 \text{ kg m}^{-2}$  ( $50 \text{ t ha}^{-1}$ ) and mixed to a depth of 12cm (for a detailed description of mesocosm design and construction, substrate and feedstock preparation and characterization, plant varieties and growth conditions, and irrigation regime, see *Supporting Information*).

Leachate was collected from mesocosms at six separate leachate events. After 235 days, samples were taken from relevant chemical pools — the soil exchangeable fraction, the solid phase with the exchangeable fraction removed, and the plant material (comprising shoots, roots and seeds). Using a conventional approach focused on reaction products, we calculated elemental budgets for cations for each mesocosm from the dissolved or non-mineral-bound pools (leachate + soil exchangeable fraction + plant material) (see *Supporting Information Section 1.9*). We compared the elemental budgets calculated for basalt-amended mesocosms to a control mesocosm for each fertilizer treatment that had no basalt applied. Control mesocosms were selected as the control replicates for which the topsoil major element composition most closely matched the initial soil baseline. The excess  $\text{Na}^+$ ,  $\text{Ca}^{2+}$ , and  $\text{Mg}^{2+}$  in the elemental budget of basalt-amended mesocosms relative to the controls were assumed to represent reaction products of basalt dissolution. From the amounts of these cations we obtained initial ERW rates. Using a modified Steinhour formulation that relates the amount of mobile cations to the amount of carbonic acidity converted to bicarbonate (see *Supporting Information Section 1.3*), ERW rates were converted to CDR estimates.

These rates can be compared with those obtained using the TiCAT method, as the cations released into non-mineral-bound pools from feedstock weathering should correspond to the amount of cation loss from the basalt fraction being weathered. We analyzed the concentration of Na, Ca, Mg and Ti in the solid phase samples taken from the upper 12cm portion of each mesocosm. We calculated  $F_D$  of the basalt fraction present in the soil + basalt mixture separately for each major cation (see Section 2.1, also *Supporting Information Section 1.10*). From the cation  $F_D$  for each mesocosm and using the application rate of basalt for each mesocosm, we calculated the total amount of cation in feedstock applied over a given area that was dissolved ( $n_i$ ; see *Supporting Information Section 1.10*), giving an initial ERW rate, and using the same modified Steinhour formulation described above, an initial CDR estimate.

### 4 Results and Discussion

Our results show agreement between two independent methods of calculating CDR in our mesocosm systems, with a systematic offset (**Fig. 3a**). The conventional approach, measuring cation reaction products in dissolved cation pools, yielded mean CDR estimates of  $1.68 \pm 0.28 \text{ tCO}_2\text{eq ha}^{-1}$  (NPK-fertilized) and  $1.05 \pm 0.39 \text{ tCO}_2\text{eq ha}^{-1}$  (manure-fertilized) across all mesocosms. The TiCAT approach introduced here, which measures cation loss from the solid phase of soil samples, gave mean CDR estimates of  $2.73 \pm 1.11 \text{ tCO}_2\text{eq ha}^{-1}$  (NPK-fertilized) and  $1.74 \pm 1.41 \text{ tCO}_2\text{eq ha}^{-1}$  (manure-fertilized). Although some offset between TiCAT estimates and those derived from dissolved cation pool budgets is to be expected given the challenges associated with obtaining representative samples from dissolved pools (see 47), mean CDR estimates from these methods were within error ( $\pm 2\sigma$ ) for both NPK- and manure-fertilized basalt-amended mesocosms.

Mean initial CDR values across all basalt-amended mesocosms were  $2.24 \pm 1.33 \text{ tCO}_2\text{eq ha}^{-1}$  (TiCAT), and  $1.36 \pm 0.46 \text{ tCO}_2\text{eq ha}^{-1}$  (dissolved pools) (**Fig. 3b**). This is broadly consistent with estimated CDR values calculated for similar ERW studies, albeit these range greatly in application amount and duration (see 33).

Given a CDR potential for the basalt used in our study of  $183.56 \text{ kgCO}_2 \text{ t}^{-1}$  (see *Supporting Information Section 1.3*), the initial CDR efficiency after 235 days was  $24.4 \pm 14.5 \%$ , using results from TiCAT. Analysis of total inorganic carbon (TIC) and ammonium acetate leaching strongly suggest that carbonate formation and exchangeable cations in basalt feedstock should have a negligible impact on the overall cation budget of the mesocosm systems (*Supporting Information*). Our results thus demonstrate that the solid-phase approach underlying TiCAT produces estimates for initial CDR within error of those calculated by analyzing the dissolved, plant, and soil exchangeable cation pools that constitute the ultimate reaction products in our mesocosm experiments, suggesting that it can yield an accurate and robust estimate of initial CDR in enhanced weathering systems.

The TiCAT method overcomes significant issues with prior methods of estimating ERW, particularly those that rely on accurately measuring the amount and transport of weathering reaction products (i.e., bicarbonate ions,  $\text{HCO}_3^-$ , or cations in soil drainage waters) after feedstock application. Methods that rely on tracking the dissolved phase are extremely time- and labor-intensive, introducing significant barriers to scale. For example, a thorough study of a field-scale ERW trial monitoring aqueous reaction products, such as that conducted by ref. 54, involves many months of labor- and time-intensive sampling not only of soils, plants, and possibly porewaters from the agricultural plots onto which ERW feedstock is applied, but also a wider detailed monitoring of the drainage regime and watershed around such a site. Even using this style of sampling protocol, the necessary granularity of measurements would likely miss short-term fluctuations such as wash-out after rain events, which in many river systems account for an important component of the overall solute discharge (e.g., 77). Such measurements can also be complicated by varying timeframes over which cations are bound to exchangeable sorption sites within a soil (see 46, 47).

Our approach also directly overcomes possibly the largest uncertainty in scaling ERW within agricultural settings — estimating the initial extent of feedstock dissolution in soils (see e.g., 33; 55). There is currently significant uncertainty on how rock grain surface areas evolve through time within a given field setting (i.e., individual farm), and the extent to which secondary mineral formation on the surface of feedstock has the potential to alter mineral dissolution rates (e.g., 78-86). In addition, bulk mineral dissolution kinetics are in some cases poorly constrained (e.g., 82, 87, 88). Taken together, these considerations make it extremely challenging to accurately forecast feedstock dissolution across a range of deployment regimes with existing reactive transport models alone (33, 55, 78-88).

A significant additional advantage to this MRV approach is that it can directly integrate into existing agronomic practices. Samples from the uppermost portion of the soil are already regularly taken for nutrient and soil pH analysis (89, 90). Importantly, this means that there is already extensive personnel and infrastructure in place that can be leveraged to scale empirical validation of carbon capture through ERW at minimal cost, in marked contrast to empirical verification of soil organic carbon concentrations (SOC), which requires modified sampling protocols for accurate empirical results. Existing frameworks for carbon storage in agricultural settings are mostly focused on SOC (e.g., the US Department of Agriculture's COMET-Farm calculator, see <http://www.comet-farm.com>), which does not allow for landowners and land users to include alkalinity generation through practices such as ERW into an estimate of carbon storage. Deployment of ERW at scale requires MRV tools such as TiCAT to be incorporated into these frameworks. This would allow for combined use of ERW and SOC maintenance to achieve maximum carbon storage depending on local conditions.

It is important to emphasize that the CDR rate estimated based on the time-integrated amount of feedstock dissolution and cation loss should be regarded as an initial CDR value. There is potential for leakage of initially captured carbon downstream of a given field deployment, as alkalinity and dissolved inorganic carbon are transported from the soil column to the oceans (e.g., 20, 57). In addition, a large fraction of the dissolved cation load in any soil will be transiently hosted in soil exchange sites (e.g., 91-93; see also 51). This cation storage at exchange sites is temporary, and upon their release dissolved cations will drive CDR through charge balance in the carbonic acid system (see 46, 47). However, there is a time-varying lag between feedstock dissolution and  $\text{CO}_2$  capture that needs to be considered for accurate CDR quantification. As a result, a robust, “cradle-to-grave” MRV approach with TiCAT at its core will also require modeling the transport of weathering products through the soil (14, 19, 43) and river-ocean system (20) to determine potential leakage through re-release of  $\text{CO}_2$  back to the atmosphere.

Lastly, effective implementation of the TiCAT approach relies on stringent constraints on analytical error, which may be challenging via standard practice with most commercially available ICP-MS measurements (see 71, 72). Nonetheless, here we have demonstrated that it is possible using isotope dilution on a standard quadrupole ICP-MS instrument to minimize analytical error to ~1%, making even <10% basalt dissolution analytically resolvable for total feedstock application rates of 50 t ha<sup>-1</sup>. However, replication of this analytical precision in commercial laboratories will require adjustment to workflows and standard operating procedures. It is also likely that the aggregate impact on unit cost (dollar cost per ton of CO<sub>2</sub> captured) of TiCAT as an MRV procedure will broadly follow a “learning curve” trajectory, driving lower costs as ERW is scaled up (e.g., 94).

## 5 Conclusion

We have demonstrated with mesocosm ERW experiments that a soil-based mass balance approach — TiCAT — accurately tracks ERW with a basalt feedstock to allow estimation of CDR rates. TiCAT yields estimates that are within error of those calculated by complete elemental budgeting of weathering reaction products gained in plant and exchangeable cation pools. Using an isotope dilution method, we can reduce analytical error sufficiently that a dissolution signal is resolvable in the solid soil phase at reasonable feedstock application rates. Applying the methods used in this study to field-scale trials is a necessary next step in verifying the capacity of TiCAT to be used for MRV in ERW in the field. Additionally, our approach will ultimately need to be augmented by the development of cradle-to-grave MRV approaches that can provide error-bounded estimates of final CDR. Nevertheless, our results suggest that the TiCAT method could be a cost-effective and accurate centerpiece of a robust MRV toolkit for deploying ERW at scale.

## Figures

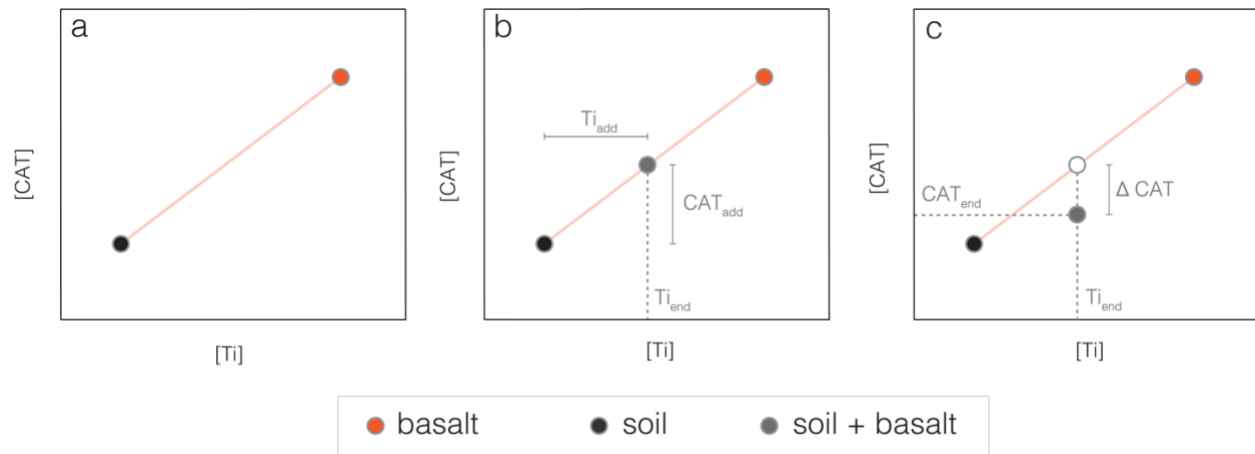


**Fig. 1.** The TiCAT conceptual framework as a simple two-component mixing model. An idealized soil and basalt endmember are plotted in Ti v CAT space (a). A mixture of soil + basalt initially plots on the idealized mixing line between both endmembers (b). Dissolution results in loss of CAT from the solid phase, while Ti is conserved as it is immobile; the original composition of the soil + basalt mixture (indicated by the white circle) is the intersection of  $Ti_{end}$  with the mixing line, and  $\Delta CAT$  is the amount of CAT lost by dissolution (c).

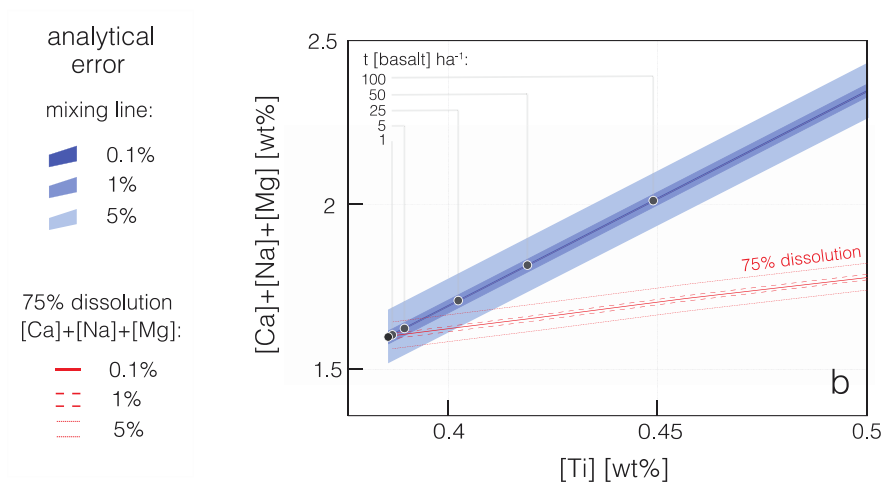
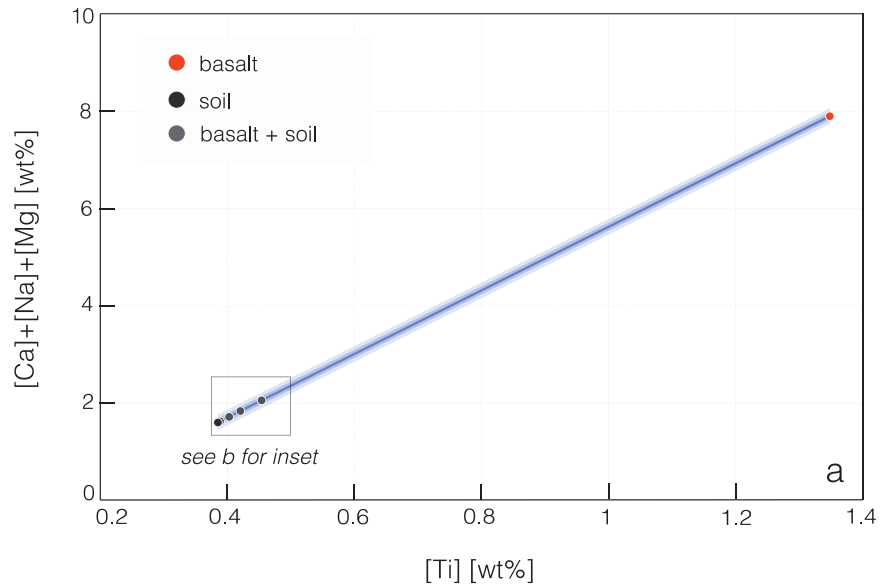


**Fig. 2.** A mixing model with representative data for soil and basalt endmembers. Assumed homogeneous mixtures of soil + basalt are shown for a range of basalt application scenarios (see inset, b). Error envelopes are shown for the mixing line and a line indicating theoretical 75% dissolution, based on potential size of analytical error on soil + basalt samples. Resolvability of a dissolution signal is dependent on dissolution rate, basalt application rate, and analytical error.

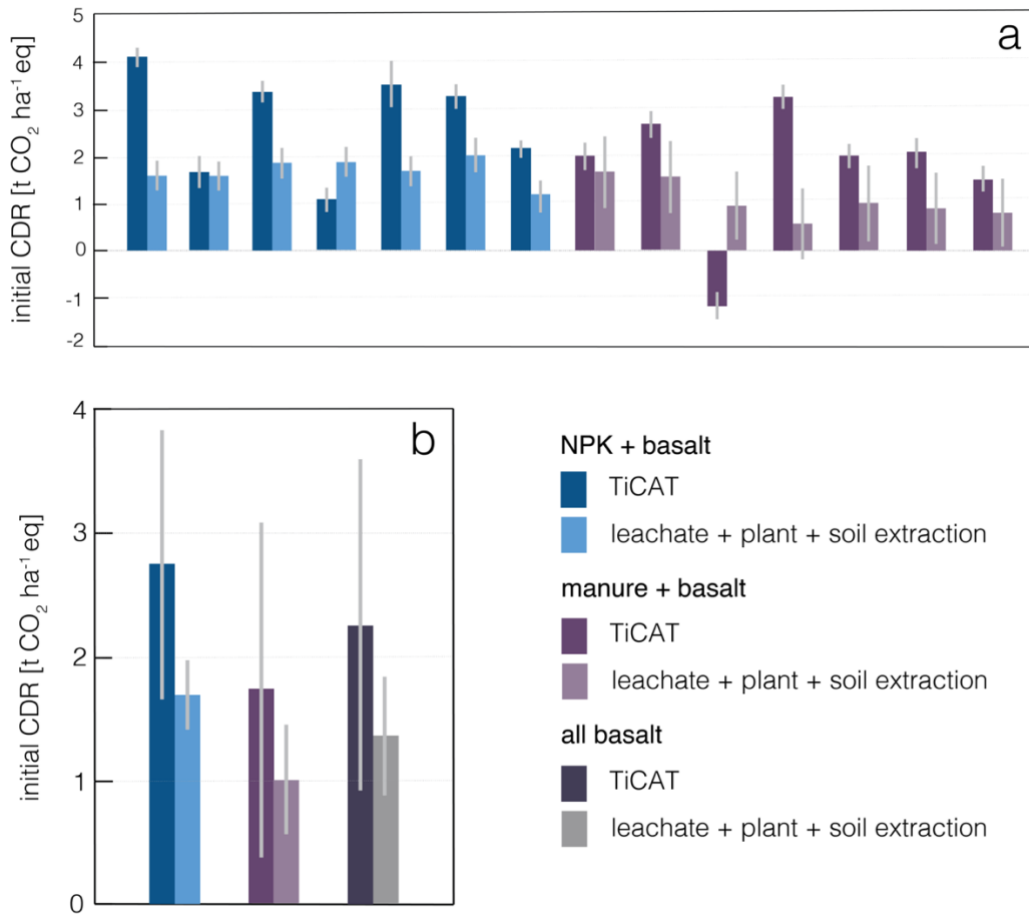


**Fig 3.** Initial CDR estimates calculated using cation data from TiCAT and from non-mineral-bound cation budgets. Results are shown for individual mesocosms (a), and as mean values for all mesocosms pooled by treatment type, where grey bars show all basalt-treated mesocosms as a single pooled data set (b). Error bars for TiCAT are propagated analytical error in (a), and standard deviation (at  $\pm 2\sigma$ ) where baseline soil and basalt samples have been pooled. Error bars for leachate + plant + soil extraction are propagated standard error between measurements for all mesocosms of the same treatment in (a), and standard deviation (at  $\pm 2\sigma$ ) where baseline soil and basalt samples have been pooled.

**Acknowledgments**

We thank Dr Amy L. Lewis for providing the basalt mineralogy and particle size distribution data for this study. We also acknowledge technical support from Irene Johnson and Dr Karen J. Bailey during soil excavation, plant tissue preparation and the ammonium acetate soil extraction. NJP acknowledges support from the Yale Center for Natural Carbon Capture. M.K. acknowledges funding through an NERC/ACCE DTP studentship and D.J.B. and D.Z.E acknowledge funding from the Leverhulme Trust through a Leverhulme Research Centre award (RC-2015-029).

## References

1. Ou, Y., Iyer, G., Clarke, L., Edmonds, J., Fawcett, A.A., Hultman, N., McFarland, J.R., Binsted, M., Cui, R., Fyson, C., Geiges, A., Gonzales-Zuñiga, S., Gidden, M.J., Höhne, N., Jeffery, L., Kuramochi, T., Lewis, J., Meinshausen, M., Nicholls, Z., Patel, P., Ragnauth, S., Rogelj, J., Waldhoff, S., Yu, S., McJeon, H., 2021. Can updated climate pledges limit warming well below 2°C? *Science* 374, 693–695. <https://doi.org/10.1126/science.abl8976>
2. Meinshausen, M., Lewis, J., McGlade, C., Gütschow, J., Nicholls, Z., Burdon, R., Cozzi, L., Hackmann, B., 2022. Realization of Paris Agreement pledges may limit warming just below 2 °C. *Nature* 604, 304–309. <https://doi.org/10.1038/s41586-022-04553-z>
3. United Nations Environment Programme, 2022. Emissions Gap Report 2022: The Closing Window — Climate crisis calls for rapid transformation of societies. Nairobi. <https://www.unep.org/emissions-gap-report-2022>
4. Lawrence, M.G., Schäfer, S., Muri, H., Scott, V., Oschlies, A., Vaughan, N.E., Boucher, O., Schmidt, H., Haywood, J., Scheffran, J., 2018. Evaluating climate geoengineering proposals in the context of the Paris Agreement temperature goals. *Nat Commun* 9, 3734. <https://doi.org/10.1038/s41467-018-05938-3>
5. IPCC, 2022. *Climate Change 2022: Mitigation of Climate Change. Contribution of Working Group III to the Sixth Assessment Report of the Intergovernmental Panel on Climate Change* [P.R. Shukla, J. Skea, R. Slade, A. Al Khourdajie, R. van Diemen, D. McCollum, M. Pathak, S. Some, P. Vyas, R. Fradera, M. Belkacemi, A. Hasija, G. Lisboa, S. Luz, J. Malley, (eds.)]. Cambridge University Press, Cambridge, UK and New York, NY, USA. doi: 10.1017/9781009157926
6. Schuiling, R.D., Krijgsman, P., 2006. Enhanced Weathering: An Effective and Cheap Tool to Sequester CO<sub>2</sub>. *Climatic Change* 74, 349–354. <https://doi.org/10.1007/s10584-005-3485-y>
7. Köhler, P., Hartmann, J., Wolf-Gladrow, D.A., 2010. Geoengineering potential of artificially enhanced silicate weathering of olivine. *Proc National Acad Sci* 107, 20228–20233. <https://doi.org/10.1073/pnas.1000545107>
8. Renforth, P., 2012. The potential of enhanced weathering in the UK. *Int J Greenh Gas Con* 10, 229–243. <https://doi.org/10.1016/j.ijggc.2012.06.011>
9. Hartmann, J., West, A.J., Renforth, P., Köhler, P., Rocha, C.L.D.L., Wolf-Gladrow, D.A., Dürr, H.H., Scheffran, J., 2013. Enhanced chemical weathering as a geoengineering strategy to reduce atmospheric carbon dioxide, supply nutrients, and mitigate ocean acidification. *Rev Geophys* 51, 113–149. <https://doi.org/10.1002/rog.20004>
10. Kantola, I.B., Masters, M.D., Beerling, D.J., Long, S.P., DeLucia, E.H., 2017. Potential of global croplands and bioenergy crops for climate change mitigation through deployment for enhanced weathering. *Biol Letters* 13, 20160714. <https://doi.org/10.1098/rsbl.2016.0714>
11. Taylor, L.L., Beerling, D.J., Quegan, S., Banwart, S.A., 2017. Simulating carbon capture by enhanced weathering with croplands: an overview of key processes highlighting areas of future model development. *Biol Letters* 13, 20160868. <https://doi.org/10.1098/rsbl.2016.0868>
12. Strefler, J., Amann, T., Bauer, N., Kriegler, E., Hartmann, J., 2018. Potential and costs of carbon dioxide removal by enhanced weathering of rocks. *Environ Res Lett* 13, 034010. <https://doi.org/10.1088/1748-9326/aaa9c4>
13. Beerling, D.J., Leake, J.R., Long, S.P., Scholes, J.D., Ton, J., Nelson, P.N., Bird, M., Kantzas, E., Taylor, L.L., Sarkar, B., Kelland, M., DeLucia, E., Kantola, I., Müller, C., Rau, G., Hansen, J., 2018. Farming with crops and rocks to address global climate, food and soil security. *Nat Plants* 4, 138–147. <https://doi.org/10.1038/s41477-018-0108-y>
14. Beerling, D.J., Kantzas, E.P., Lomas, M.R., Wade, P., Eufrazio, R.M., Renforth, P., Sarkar, B., Andrews, M.G., James, R.H., Pearce, C.R., Mercure, J.-F., Pollitt, H., Holden, P.B., Edwards, N.R., Khanna, M., Koh, L., Quegan, S., Pidgeon, N.F., Janssens, I.A., Hansen, J., Banwart, S.A., 2020. Potential for large-scale CO<sub>2</sub> removal via enhanced rock weathering with croplands. *Nature* 583, 242–248. <https://doi.org/10.1038/s41586-020-2448-9>
15. Taylor, L.L., Quirk, J., Thorley, R.M.S., Kharecha, P.A., Hansen, J., Ridgwell, A., Lomas, M.R., Banwart, S.A., Beerling, D.J., 2016. Enhanced weathering strategies for stabilizing climate and averting ocean acidification. *Nat Clim Change* 6, 402–406. <https://doi.org/10.1038/nclimate2882>

16. Edwards, D.P., Lim, F., James, R.H., Pearce, C.R., Scholes, J., Freckleton, R.P., Beerling, D.J., 2017. Climate change mitigation: potential benefits and pitfalls of enhanced rock weathering in tropical agriculture. *Biol Letters* 13, 20160715. <https://doi.org/10.1098/rsbl.2016.0715>
17. Goll, D.S., Ciais, P., Amann, T., Buermann, W., Chang, J., Eker, S., Hartmann, J., Janssens, I., Li, W., Obersteiner, M., Penuelas, J., Tanaka, K., Vicca, S., 2021. Potential CO<sub>2</sub> removal from enhanced weathering by ecosystem responses to powdered rock. *Nat Geosci* 14, 545–549. <https://doi.org/10.1038/s41561-021-00798-x>
18. Rinder, T., von Hagke, C., 2021. The influence of particle size on the potential of enhanced basalt weathering for carbon dioxide removal - Insights from a regional assessment. *J Clean Prod* 315, 128178. <https://doi.org/10.1016/j.jclepro.2021.128178>
19. Kantzas, E.P., Martin, M.V., Lomas, M.R., Eufrazio, R.M., Renforth, P., Lewis, A.L., Taylor, L.L., Mecure, J.-F., Pollitt, H., Vercoulen, P.V., Vakilifard, N., Holden, P.B., Edwards, N.R., Koh, L., Pidgeon, N.F., Banwart, S.A., Beerling, D.J., 2022. Substantial carbon drawdown potential from enhanced rock weathering in the United Kingdom. *Nat Geosci* 15, 382–389. <https://doi.org/10.1038/s41561-022-00925-2>
20. Zhang, S., Planavsky, N.J., Katchinoff, J., Raymond, P.A., Kanzaki, Y., Reershemius, T., Reinhard, C.T., 2022. River chemistry constraints on the carbon capture potential of surficial enhanced rock weathering. *Limnol Oceanogr*. <https://doi.org/10.1002/lno.12244>
21. Middelburg, J. J., Soetaert, K., Hagens, M., 2020. Ocean Alkalinity, Buffering and Biogeochemical Processes. *Reviews of Geophysics*, 58(3), e2019RG000681. <https://doi.org/10.1029/2019rg000681>
22. Urey, H. C., 1952. On the Early Chemical History of the Earth and the Origin of Life. *Proceedings of the National Academy of Sciences*, 38(4), 351–363. <https://doi.org/10.1073/pnas.38.4.351>
23. Berner, R. A., Lasaga, A. C., Garrels, R. M., 1983. The carbonate-silicate geochemical cycle and its effect on atmospheric carbon dioxide over the past 100 million years. *American Journal of Science*, 283(7), 641–683. <https://doi.org/10.2475/ajs.283.7.641>
24. Isson, T. T., Planavsky, N. J., Coogan, L. A., Stewart, E. M., Ague, J. J., Bolton, E. W., Zhang, S., McKenzie, N. R., Kump, L. R., 2020. Evolution of the Global Carbon Cycle and Climate Regulation on Earth. *Global Biogeochemical Cycles*, 34(2). <https://doi.org/10.1029/2018gb006061>
25. Smith, P., 2016. Soil carbon sequestration and biochar as negative emission technologies. *Global Change Biol* 22, 1315–1324. <https://doi.org/10.1111/gcb.13178>
26. Schlesinger, W.H., Amundson, R., 2019. Managing for soil carbon sequestration: Let's get realistic. *Global Change Biol* 25, 386–389. <https://doi.org/10.1111/gcb.14478>
27. Bossio, D.A., Cook-Patton, S.C., Ellis, P.W., Fargione, J., Sanderman, J., Smith, P., Wood, S., Zomer, R.J., Unger, M. von, Emmer, I.M., Griscom, B.W., 2020. The role of soil carbon in natural climate solutions. *Nat Sustain* 3, 391–398. <https://doi.org/10.1038/s41893-020-0491-z>
28. ten Berge, H.F.M., Meer, H.G. van der, Steenhuizen, J.W., Goedhart, P.W., Knops, P., Verhagen, J., 2012. Olivine Weathering in Soil, and Its Effects on Growth and Nutrient Uptake in Ryegrass (*Lolium perenne* L.): A Pot Experiment. *Plos One* 7, e42098. <https://doi.org/10.1371/journal.pone.0042098>
29. Song, Z., Liu, C., Müller, K., Yang, X., Wu, Y., Wang, H., 2018. Silicon regulation of soil organic carbon stabilization and its potential to mitigate climate change. *Earth-sci Rev* 185, 463–475. <https://doi.org/10.1016/j.earscirev.2018.06.020>
30. Amann, T., Hartmann, J., Struyf, E., Garcia, W. de O., Fischer, E.K., Janssens, I., Meire, P., Schoelynck, J., 2020. Enhanced Weathering and related element fluxes – a cropland mesocosm approach. *Biogeosciences* 17, 103–119. <https://doi.org/10.5194/bg-17-103-2020>
31. Garcia, W. de O., Amann, T., Hartmann, J., Karstens, K., Popp, A., Boysen, L.R., Smith, P., Goll, D., 2020. Impacts of enhanced weathering on biomass production for negative emission technologies and soil hydrology. *Biogeosciences* 17, 2107–2133. <https://doi.org/10.5194/bg-17-2107-2020>
32. Kelland, M.E., Wade, P.W., Lewis, A.L., Taylor, L.L., Sarkar, B., Andrews, M.G., Lomas, M.R., Cotton, T.E.A., Kemp, S.J., James, R.H., Pearce, C.R., Hartley, S.E., Hodson, M.E., Leake, J.R., Banwart, S.A., Beerling, D.J., 2020. Increased yield and CO<sub>2</sub> sequestration potential with the C4 cereal *Sorghum bicolor* cultivated in basaltic rock dust-amended agricultural soil. *Global Change Biol* 26, 3658–3676. <https://doi.org/10.1111/gcb.15089>

33. Swoboda, P., Döring, T.F., Hamer, M., 2021. Remineralizing soils? The agricultural usage of silicate rock powders: A review. *Sci Total Environ* 807, 150976. <https://doi.org/10.1016/j.scitotenv.2021.150976>
34. Davies, B., Finney, B., Eagle, D., 2001. *Resource Management: Soil*. Farming Press, ISBN 0 85236 559 4.
35. Kamprath, E.J., Smyth, T.J., 2005. Liming. In: Hillel, D. (ed.). *Encyclopedia of Soils in the Environment*. Elsevier, ISBN 9780123485304, 350-358, <https://doi.org/10.1016/B0-12-348530-4/00225-3>
36. Goulding, K.W.T., 2016. Soil acidification and the importance of liming agricultural soils with particular reference to the United Kingdom. *Soil Use Manage*, 32: 390-399. <https://doi.org/10.1111/sum.12270>
37. Semhi, K., Suchet, P.A., Clauer, N., Probst, J.-L., 2000. Impact of nitrogen fertilizers on the natural weathering-erosion processes and fluvial transport in the Garonne basin. *Appl Geochem* 15, 865–878. [https://doi.org/10.1016/s0883-2927\(99\)00076-1](https://doi.org/10.1016/s0883-2927(99)00076-1)
38. West, T.O., McBride, A.C., 2005. The contribution of agricultural lime to carbon dioxide emissions in the United States: dissolution, transport, and net emissions. *Agric Ecosyst Environ* 108, 145–154. <https://doi.org/10.1016/j.agee.2005.01.002>
39. Oh, N., Raymond, P.A., 2006. Contribution of agricultural liming to riverine bicarbonate export and CO<sub>2</sub> sequestration in the Ohio River basin. *Global Biogeochem Cy* 20, n/a-n/a. <https://doi.org/10.1029/2005gb002565>
40. Hamilton, S.K., Kurzman, A.L., Arango, C., Jin, L., Robertson, G.P., 2007. Evidence for carbon sequestration by agricultural liming. *Global Biogeochem Cy* 21, n/a-n/a. <https://doi.org/10.1029/2006gb002738>
41. Perrin, A.-S., Probst, A., Probst, J.-L., 2008. Impact of nitrogenous fertilizers on carbonate dissolution in small agricultural catchments: Implications for weathering CO<sub>2</sub> uptake at regional and global scales. *Geochim Cosmochim Acta* 72, 3105–3123. <https://doi.org/10.1016/j.gca.2008.04.011>
42. Dietzen, C., Harrison, R., Michelsen-Correa, S., 2018. Effectiveness of enhanced mineral weathering as a carbon sequestration tool and alternative to agricultural lime: An incubation experiment. *Int J Greenh Gas Con* 74, 251–258. <https://doi.org/10.1016/j.ijggc.2018.05.007>
43. Kanzaki, Y., Zhang, S., Planavsky, N.J., Reinhard, C.T., 2022. Soil Cycles of Elements simulator for Predicting TERrestrial regulation of greenhouse gases: SCEPTER v0.9. *Geoscientific Model Dev Discuss* 2022, 1–58. <https://doi.org/10.5194/gmd-2022-8>
44. Cipolla, G., Calabrese, S., Noto, L.V., Porporato, A., 2021. The role of hydrology on enhanced weathering for carbon sequestration I. Modeling rock-dissolution reactions coupled to plant, soil moisture, and carbon dynamics. *Adv Water Resour* 154, 103934. <https://doi.org/10.1016/j.advwatres.2021.103934>
45. Renforth, P., Pogge von Strandmann, P.A.E., Henderson, G.M., 2015. The dissolution of olivine added to soil: Implications for enhanced weathering. *Appl Geochem* 61, 109–118. <https://doi.org/10.1016/j.apgeochem.2015.05.016>
46. Pogge von Strandmann, P.A.E., Fraser, W.T., Hammond, S.J., Tarbuck, G., Wood, I.G., Oelkers, E.H., Murphy, M.J., 2019. Experimental determination of Li isotope behaviour during basalt weathering. *Chem Geol* 517, 34–43. <https://doi.org/10.1016/j.chemgeo.2019.04.020>
47. Pogge von Strandmann, P.A.E., Renforth, P., West, A.J., Murphy, M.J., Luu, T.-H., Henderson, G.M., 2021. The lithium and magnesium isotope signature of olivine dissolution in soil experiments. *Chem Geol* 560, 120008. <https://doi.org/10.1016/j.chemgeo.2020.120008>
48. Pogge von Strandmann, P.A.E., Tooley, C., Mulders, J.J.P.A., Renforth, P., 2022. The Dissolution of Olivine Added to Soil at 4°C: Implications for Enhanced Weathering in Cold Regions. *Frontiers Clim* 4. <https://doi.org/10.3389/fclim.2022.827698>
49. Amann, T., Hartmann, J., Hellmann, R., Pedrosa, E.T., Malik, A., 2022. Enhanced weathering potentials—the role of in situ CO<sub>2</sub> and grain size distribution. *Frontiers Clim* 4, 929268. <https://doi.org/10.3389/fclim.2022.929268>
50. Jariwala, H., Haque, F., Vanderburgt, S., Santos, R.M., Chiang, Y.W., 2022. Mineral–Soil–Plant–Nutrient Synergisms of Enhanced Weathering for Agriculture: Short-Term Investigations Using Fast-Weathering Wollastonite Skarn. *Front Plant Sci* 13, 929457. <https://doi.org/10.3389/fpls.2022.929457>

51. Vienne, A., Poblador, S., Portillo-Estrada, M., Hartmann, J., Ijehon, S., Wade, P., Vicca, S., 2022. Enhanced Weathering Using Basalt Rock Powder: Carbon Sequestration, Co-benefits and Risks in a Mesocosm Study With *Solanum tuberosum*. *Frontiers Clim* 4, 869456. <https://doi.org/10.3389/fclim.2022.869456>
52. Haque, F., Santos, R.M., Chiang, Y.W., 2020. CO<sub>2</sub> sequestration by wollastonite-amended agricultural soils – An Ontario field study. *Int J Greenh Gas Con* 97, 103017. <https://doi.org/10.1016/j.ijggc.2020.103017>
53. Taylor, L.L., Driscoll, C.T., Groffman, P.M., Rau, G.H., Blum, J.D., Beerling, D.J., 2021. Increased carbon capture by a silicate-treated forested watershed affected by acid deposition. *Biogeosciences* 18, 169–188. <https://doi.org/10.5194/bg-18-169-2021>
54. Larkin, C.S., Andrews, M.G., Pearce, C.R., Yeong, K.L., Beerling, D.J., Bellamy, J., Benedick, S., Freckleton, R.P., Goring-Harford, H., Sadekar, S., James, R.H., 2022. Quantification of CO<sub>2</sub> removal in a large-scale enhanced weathering field trial on an oil palm plantation in Sabah, Malaysia. *Frontiers Clim* 4, 959229. <https://doi.org/10.3389/fclim.2022.959229>
55. Calabrese, S., Wild, B., Bertagni, M.B., Bourg, I.C., White, C., Aburto, F., Cipolla, G., Noto, L.V., Porporato, A., 2022. Nano- to Global-Scale Uncertainties in Terrestrial Enhanced Weathering. *Environ Sci Technol*. <https://doi.org/10.1021/acs.est.2c03163>
56. Almaraz, M., Bingham, N.L., Holzer, I.O., Geoghegan, E.K., Goertzen, H., Sohng, J., Houlton, B.Z., 2022. Methods for determining the CO<sub>2</sub> removal capacity of enhanced weathering in agronomic settings. *Frontiers Clim* 4, 970429. <https://doi.org/10.3389/fclim.2022.970429>
57. Chay, F., Klitzke, J., Hausfather, Z., Martin, K., Freeman, J., Cullenward, D., 2022. Verification Confidence Levels for carbon dioxide removal. *CarbonPlan* <https://carbonplan.org/research/cdr-verification-explainer>
58. Brimhall, G.H., Dietrich, W.E., 1987. Constitutive mass balance relations between chemical composition, volume, density, porosity, and strain in metasomatic hydrochemical systems: Results on weathering and pedogenesis. *Geochim Cosmochim Acta* 51, 567–587. [https://doi.org/10.1016/0016-7037\(87\)90070-6](https://doi.org/10.1016/0016-7037(87)90070-6)
59. Chadwick, O.A., Brimhall, G.H., Hendricks, D.M., 1990. From a black to a gray box — a mass balance interpretation of pedogenesis. *Geomorphology* 3, 369–390. [https://doi.org/10.1016/0169-555x\(90\)90012-f](https://doi.org/10.1016/0169-555x(90)90012-f)
60. Chadwick, O.A., Derry, L.A., Vitousek, P.M., Huebert, B.J., Hedin, L.O., 1999. Changing sources of nutrients during four million years of ecosystem development. *Nature* 397, 491–497. <https://doi.org/10.1038/17276>
61. Brimhall, G.H., J., L.C., Ford, C., Bratt, J., Taylor, G., Warin, O., 1991. Quantitative geochemical approach to pedogenesis: importance of parent material reduction, volumetric expansion, and eolian influx in lateritization. *Geoderma* 51, 51–91. [https://doi.org/10.1016/0016-7061\(91\)90066-3](https://doi.org/10.1016/0016-7061(91)90066-3)
62. Kurtz, A.C., Derry, L.A., Chadwick, O.A., Alfano, M.J., 2000. Refractory element mobility in volcanic soils. *Geology* 28, 683–686. [https://doi.org/10.1130/0091-7613\(2000\)28<683:remivs>2.0.co;2](https://doi.org/10.1130/0091-7613(2000)28<683:remivs>2.0.co;2)
63. White, A.F., Bullen, T.D., Schulz, M.S., Blum, A.E., Huntington, T.G., Peters, N.E., 2001. Differential rates of feldspar weathering in granitic regoliths. *Geochim Cosmochim Acta* 65, 847–869. [https://doi.org/10.1016/s0016-7037\(00\)00577-9](https://doi.org/10.1016/s0016-7037(00)00577-9)
64. Anderson, S.P., Dietrich, W.E., Brimhall, G.H., 2002. Weathering profiles, mass-balance analysis, and rates of solute loss: Linkages between weathering and erosion in a small, steep catchment. *Gsa Bulletin* 114, 1143–1158. [https://doi.org/10.1130/0016-7606\(2002\)114<1143:wpmbaa>2.0.co;2](https://doi.org/10.1130/0016-7606(2002)114<1143:wpmbaa>2.0.co;2)
65. Riebe, C.S., Kirchner, J.W., Finkel, R.C., 2003. Long-term rates of chemical weathering and physical erosion from cosmogenic nuclides and geochemical mass balance. *Geochim Cosmochim Acta* 67, 4411–4427. [https://doi.org/10.1016/s0016-7037\(03\)00382-x](https://doi.org/10.1016/s0016-7037(03)00382-x)
66. Tabor, N.J., Montañez, I.P., Zierenberg, R., Currie, B.S., 2004. Mineralogical and geochemical evolution of a basalt-hosted fossil soil (Late Triassic, Ischigualasto Formation, northwest Argentina): Potential for paleoenvironmental reconstruction. *Gsa Bulletin* 116, 1280–1293. <https://doi.org/10.1130/b25222.1>
67. Sheldon, N.D., Tabor, N.J., 2009. Quantitative paleoenvironmental and paleoclimatic reconstruction using paleosols. *Earth-sci Rev* 95, 1–52. <https://doi.org/10.1016/j.earscirev.2009.03.004>

68. Brantley, S.L., Lebedeva, M., 2011. Learning to Read the Chemistry of Regolith to Understand the Critical Zone. *Annu Rev Earth Pl Sc* 39, 387–416. <https://doi.org/10.1146/annurev-earth-040809-152321>
69. Fisher, B.A., Rendahl, A.K., Aufdenkampe, A.K., Yoo, K., 2017. Quantifying weathering on variable rocks, an extension of geochemical mass balance: Critical zone and landscape evolution. *Earth Surf. Process. Landforms* 42, 2457–2468. <https://doi.org/10.1002/esp.4212>
70. Lipp, A.G., Shorttle, O., Sperling, E.A., Brocks, J.J., Cole, D.B., Crockford, P.W., Mouro, L.D., Dewing, K., Dornbos, S.Q., Emmings, J.F., Farrell, U.C., Jarrett, A., Johnson, B.W., Kabanov, P., Keller, C.B., Kunzmann, M., Miller, A.J., Mills, N.T., O'Connell, B., Peters, S.E., Planavsky, N.J., Ritzer, S.R., Schoepfer, S.D., Wilby, P.R., Yang, J., 2021. The composition and weathering of the continents over geologic time. *Geochem Perspectives Lett* 21–26. <https://doi.org/10.7185/geochemlet.2109>
71. Andersen, J.E.T., 2014. On the development of quality assurance. *Trac Trends Anal Chem* 60, 16–24. <https://doi.org/10.1016/j.trac.2014.04.016>
72. Eggen, O.A., Reimann, C., Flem, B., 2019. Reliability of geochemical analyses: Deja vu all over again. *Sci Total Environ* 670, 138–148. <https://doi.org/10.1016/j.scitotenv.2019.03.185>
73. Inghram, M.G., 1954. Stable isotope dilution as an analytical tool. *Ann Rev Nucl Sci* 4:1, 81-92. <https://doi.org/10.1146/annurev.ns.04.120154.000501>
74. Evans, E.H., Clough, R., 2005. Isotope dilution analysis. In: Worsfold, P., Townshend, A., Poole, C. (eds.). *Encyclopedia of Analytical Science* (2<sup>nd</sup> ed.). Elsevier, 545-553. <https://doi.org/10.1016/B0-12-369397-7/00301-0>
75. Stracke, A., Scherer, E.E., Reynolds, B.C., 2014. Application of isotope dilution in geochemistry. *Treatise on Geochemistry* (Second Edition) 71–86. <https://doi.org/10.1016/b978-0-08-095975-7.01404-2>
76. Willbold, M., Jochum, K.P., 2005. Multi-Element Isotope Dilution Sector Field ICP-MS: A Precise Technique for the Analysis of Geological Materials and its Application to Geological Reference Materials. *Geostand Geoanal Res* 29, 63–82. <https://doi.org/10.1111/j.1751-908x.2005.tb00656.x>
77. Raymond, P.A., Saiers, J.E., Sobczak, W.V., 2016. Hydrological and biogeochemical controls on watershed dissolved organic matter transport: pulse-shunt concept. *Ecology* 97, 5–16. <https://doi.org/10.1890/14-1684.1>
78. Siever, R., Woodford, N., 1979. Dissolution kinetics and the weathering of mafic minerals. *Geochim Cosmochim Acta* 43, 717–724. [https://doi.org/10.1016/0016-7037\(79\)90255-2](https://doi.org/10.1016/0016-7037(79)90255-2)
79. Velbel, M.A., 1986. Influence of surface area, surface characteristics, and solution composition on feldspar weathering rates. In: J.A. Davis, K.F. Hayes (eds.), *Geochemical Processes at Mineral Surfaces*, American Chemical Society Symposium Series No. 323, pp. 615-634
80. White, A.F., Peterson, M.L., 1990. Chemical Modeling of Aqueous Systems II. *Acs Sym Ser* 461–475. <https://doi.org/10.1021/bk-1990-0416.ch035>
81. Nugent, M.A., Brantley, S.L., Pantano, C.G., Maurice, P.A., 1998. The influence of natural mineral coatings on feldspar weathering. *Nature* 395, 588–591. <https://doi.org/10.1038/26951>
82. White, A.F., Brantley, S.L., 2003. The effect of time on the weathering of silicate minerals: why do weathering rates differ in the laboratory and field? *Chem Geol* 202, 479–506. <https://doi.org/10.1016/j.chemgeo.2003.03.001>
83. Béarat, H., McKelvy, M.J., Chizmeshya, A.V.G., Gormley, D., Nunez, R., Carpenter, R.W., Squires, K., Wolf, G.H., 2006. Carbon Sequestration via Aqueous Olivine Mineral Carbonation: Role of Passivating Layer Formation. *Environ Sci Technol* 40, 4802–4808. <https://doi.org/10.1021/es0523340>
84. Daval, D., Calvaruso, C., Guyot, F., Turpault, M.-P., 2018. Time-dependent feldspar dissolution rates resulting from surface passivation: Experimental evidence and geochemical implications. *Earth Planet Sc Lett* 498, 226–236. <https://doi.org/10.1016/j.epsl.2018.06.035>
85. Zhu, C., Lu, P., 2009. Alkali feldspar dissolution and secondary mineral precipitation in batch systems: 3. Saturation states of product minerals and reaction paths. *Geochim Cosmochim Acta* 73, 3171–3200. <https://doi.org/10.1016/j.gca.2009.03.015>
86. Emmanuel, S., Ague, J.J., 2011. Impact of nano-size weathering products on the dissolution rates of primary minerals. *Chem Geol* 282, 11–18. <https://doi.org/10.1016/j.chemgeo.2011.01.002>

87. White, A.F., Schulz, M.S., Lawrence, C.R., Vivit, D.V., Stonestrom, D.A., 2017. Long-term flow-through column experiments and their relevance to natural granitoid weathering rates. *Geochim Cosmochim Acta* 202, 190–214. <https://doi.org/10.1016/j.gca.2016.11.042>
88. Brantley, S.L., Shaughnessy, A., Lebedeva, M.I., Balashov, V.N., 2023. How temperature-dependent silicate weathering acts as Earth's geological thermostat. *Science* 379, 382–389. <https://doi.org/10.1126/science.add2922>
89. Austin, R., Gatiboni, L., Havlin, J., 2020. Soil Sampling Strategies for Site-Specific Field Management. NC State Extensions, <https://content.ces.ncsu.edu/soil-sampling-strategies-for-site-specific-field-management>
90. Allen, W.J., Sapsford, S.J., Dickie, I.A., 2021. Soil sample pooling generates no consistent inference bias: a meta-analysis of 71 plant–soil feedback experiments. *New Phytol* 231, 1308–1315. <https://doi.org/10.1111/nph.17455>
91. Carroll, D., 1959. Ion exchange in clays and other minerals. *GSA Bulletin* 70, 749–779. [https://doi.org/10.1130/0016-7606\(1959\)70\[749:ieicao\]2.0.co;2](https://doi.org/10.1130/0016-7606(1959)70[749:ieicao]2.0.co;2)
92. Sumner, M.E., Miller, W.P., 1996. Cation Exchange Capacity and Exchange Coefficients. In: Sparks, D.L. (ed.), *Methods of Soil Analysis Part 3: Chemical Methods*, SSSA Book Series 5, Soil Science Society of America, Madison, Wisconsin, 1201-1230.
93. Sparks, D.L., 2003. *Environmental soil chemistry* (2<sup>nd</sup> ed.). Academic Press, ISBN 9780126564464, <https://doi.org/10.1016/B978-012656446-4/50006-2>.
94. Kahouli-Brahmi, S., 2008. Technological learning in energy–environment–economy modelling: A survey. *Energ Policy* 36, 138–162. <https://doi.org/10.1016/j.enpol.2007.09.001>

## Supporting Information Text

### 1 Supplemental Materials and Methods

**1.1 Mesocosm design and construction.** Replicated mesocosms (**Fig. S1a**) ( $n = 7$ ) for the four soil treatments in this study (NPK –basalt, NPK +basalt, manure –basalt, manure +basalt) were constructed from two sections of polyvinyl chloride (PVC) pipe, joined by a pair of PVC endcaps fixed in a back-to-back arrangement (152 mm internal diameter pipe, 160 mm internal diameter endcaps; Brett Martin, Newtownabbey, UK). The freestanding mesocosms were stabilised with a 170 mm × 190 mm acrylic baseplate fixed to a further 160 mm internal diameter endcap that was attached to the lower pipe section. Weight-bearing external joints were secured with PVC weld cement (Tangit ABS; Henkel, Düsseldorf, Germany) and internal seals were formed from high-strength polyurethane sealant (PU18; Bond It Ltd, Elland, UK).

Substrate was loaded into the 600 mm long top section and leachate collection apparatus were housed in the 400 mm long lower section. The joint attaching these pipe sections was fitted with a 20 mm internal diameter nylon nozzle to direct leachate into a high-density polyethylene bottle via a polypropylene funnel (1 L narrow-neck polyethylene bottle, 150 mm lightweight polypropylene filter funnel; Azlon, Stoke-on-Trent, UK). Soil particle migration into the leachate nozzle was reduced by emplacing a 60 mm deep drainage layer in the base of the substrate-holding top section, comprised of 20 mm diameter polyoxymethylene balls (Bearing Warehouse Ltd, Sheffield, UK). A detachable 3-ply opaque mylar membrane (Reflex Total Blackout; GroWell Horticulture Ltd, Sheffield, UK) was used to reduce algal growth in the leachate collection apparatus.

**1.2 Substrate preparation and characterization.** Mildly acidic (pH 6.45) agricultural soil of clay-loam texture (29.0, 34.3 and 36.7% by mass of clay (<2 µm), silt (2-60 µm) and sand (60-2,000 µm), respectively) was collected from farmland under *Brassica napus* (oil seed rape) cultivation at the Game and Wildlife Conservation Trust, Allerton Project, Leicestershire, UK (latitude 52.611286 °N, longitude 0.831559 °W). The soil had an initial cation exchange capacity of 22.0 cmol (p<sup>+</sup>) kg<sup>-1</sup>, with a base saturation of 70.0%, calcium saturation of 63.4%, and a gravimetric water content (GWC) at field capacity of 0.68 g g<sup>-1</sup>. The soil total carbon concentration was 2.3 wt% and the soil organic carbon concentration was 1.1 wt%.

Collected soil was manually comminuted at 18°C and stored in partially sealed polypropylene bags to reduce moisture loss. Large stones and invertebrates were removed before the soil was passed through a woven stainless-steel sieve (2 mm mesh size; Fisher Scientific UK Ltd, Loughborough, UK). After comminution, the soil had a GWC of 0.28 g g<sup>-1</sup>. Organic fertilizer for the experiment was derived from cow manure collected from Hope Farm, Hassop, UK. The manure was air dried for 30 days, then manually comminuted at 18 °C and passed through a 2 mm mesh size stainless-steel sieve.

Mesocosms were filled with substrate in a sub- and top-soil arrangement to simulate a tillage regime (3:1 mass ratio of sub- to top-soil) (**Fig. S1b**). The total dry mass of soil in each mesocosm was 8.252 kg, which – being compacted to a column height of 500 mm – had an average bulk density of 0.91 kg L<sup>-1</sup>. Basalt and fertilizer were added, as required, to the topsoil only and were mixed thoroughly into the substrate immediately prior to mesocosm filling on day 0. A total mass of 91 g (equivalent to 5.0 kg m<sup>-2</sup>) of basalt (see below) was added to treated mesocosms. Soils treated with chemical fertilizer received individually weighed quantities of analytical-grade compounds (0.347 g of urea, 1.633 g of powdered diammonium phosphate and 1.482 g of powdered potassium chloride), which were estimated to compensate for soil nutrient losses to the crop and leachate during the experiment. Mesocosms treated with organic fertilizer received 17.7 g (equivalent to 1.0 kg m<sup>-2</sup>) of air-dried cow manure, which contained 2.57, 1.23 and 3.08% total nitrogen, phosphorus pentoxide and potassium oxide, respectively. The manure application rate was calculated to approximately equal the total nitrogen application rate in the chemical fertilizer treatment, being 25 g N m<sup>-2</sup> (250 kg N ha<sup>-1</sup>).

Initial soil pH was measured using a Jenway 3540 Bench Combined Conductivity/pH Meter (Jenway, Stone, UK) calibrated with standard solutions at pH 4, 7 and 14. Prior to pH determination, 15 g of air-dried soil was thoroughly mixed with 30 ml of deionized water in a 100 ml borosilicate glass beaker using a glass stirrer. The solution was then left for 30 minutes before recording the pH of the slurry to 0.01 pH units. Soil carbon measurements were made using a Vario EL Cube Carbon-Nitrogen Analyzer (Elementar, Stockport, UK), with soil organic carbon content determined by comparing carbon concentrations before and after soil treatment with 6 M HCl (soil:acid ratio of 90 mg to 0.5 mL).

**1.3 Basaltic rock preparation and characterization.** Crushed basalt of middle Miocene age and belonging to the 'Prineville Chemical Type Unit' of the Columbia River Basalt was sourced from the Cascade Range, Oregon (Central Oregon Basalt Products LLC, Madras, ORE, USA). The basalt was passed through a series of stainless-steel sieves of decreasing mesh size (250 µm, 100 µm and 50 µm mesh size), suspended in analytical-grade ethanol and sonicated for 30 minutes in a 5 L Pyrex beaker to separate submicron particles from larger grains. The suspension was then left for 24 h (sufficient to settle particles with diameters > 1 µm) after which the supernatant was decanted and the settled basalt material was exposed to the air for 72 h to evaporate the residual ethanol. The particle size distribution of the treated basalt was measured using an LA-950 laser diffraction particle size distribution analyzer (Horiba UK Ltd, Northampton, UK), where the particle diameter range was found to be 1.5-300 µm and the *p*80 value (the size at which 80% of the particles have diameters less than or equal to) was 35 µm (**Fig.S2**). Specific surface area of the treated basalt was determined using an Anton Paar Nova 800 Brunauer Emmett Tell (BET) surface area analyzer in the Yale Geochemistry Center and found to be 10.22 m<sup>2</sup> g<sup>-1</sup>. Error was estimated to be 0.01 m<sup>2</sup> g<sup>-1</sup>, based on a 5-point analysis. The mineralogy of the basalt (**Fig. S3**) was determined using X-ray diffraction (XRD) analysis at the British Geological Survey (BGS) Keyworth laboratories, following the protocol reported in ref. 1.

The carbon dioxide removal potential of the basalt feedstock,  $E_{pot}$  (i.e. the maximum amount of carbon dioxide consumed if all basalt were to react with proton equivalents from carbonic acid), can be quantified using a modified Steiour formulation, which relates maximum theoretical carbon dioxide reaction with elemental composition of silicate feedstocks (2; see e.g., 3-6). The Steiour formulation using major cations for alkaline minerals is given as:

$$E_{pot} = \frac{\eta M_{CO_2}}{100} * \left( \frac{\alpha CaO}{M_{CaO}} + \frac{\beta MgO}{M_{MgO}} + \frac{\varepsilon Na_2O}{M_{Na_2O}} + \frac{\theta K_2O}{M_{K_2O}} \right) , \quad (S1)$$

where  $M_i$  is molar mass;  $\eta$ ,  $\alpha$ ,  $\beta$ ,  $\varepsilon$ , and  $\theta$  are stoichiometric constants (in this case with values 2.0, 1.0, 1.0, 1.0, and 1.0 respectively); and CaO, MgO, Na<sub>2</sub>O and K<sub>2</sub>O are abundances of major oxides in the feedstock. Using this formulation, with the values for major oxide abundance given in **Table S1**,  $E_{pot}$  for the basalt feedstock used here is 211.81 kgCO<sub>2</sub> t<sup>-1</sup>. This assessment is a conservative estimate representing incongruent dissolution (i.e., does not include cations that will react to form secondary minerals, including Al<sup>3+</sup> and Fe<sup>2+</sup>; e.g., 7). Note that some previous authors have simplified this formulation to only include CaO and MgO, when assessing  $E_{pot}$  for fast-weathering Ca- and Mg-silicates (e.g., 8), which are the most abundant cations. In this study, we ignore the contribution of K<sup>+</sup> to carbon dioxide removal, due to its presence in NPK fertilizers; as such, when excluding K<sub>2</sub>O,  $E_{pot}$  for the basalt feedstock is revised to 183.56 kgCO<sub>2</sub> t<sup>-1</sup>.

**1.4 Plant varieties and growth conditions.** A single specimen of dwarf hybrid *Sorghum bicolor* (Pennsylvania 115, Oakbank Game and Conservation, Cambridgeshire, UK) was cultivated in each mesocosm. Approximately 600 seeds were germinated on filter paper (Whatman #1; Cytiva, Sheffield, UK) moistened with distilled water, placed in grip seal polyethylene bags and incubated at 25°C in darkness for 24 h. 144 seeds of similar radicle length (ca. 5 mm) were selected for planting in 24-cell seed trays containing soil from the same field site. Seed trays were transferred to a growth room and maintained at 60–70% relative humidity, with an 18 h day length and 25/17°C day/night temperatures. After 24 h, 87 seedlings emerged from the soil, of which the 28

largest were grown for a further 9 d and chosen at random for transplantation to mesocosms on day 0.

Additive CO<sub>2</sub> was used to sustain atmospheric concentrations of 400 ppm in the controlled environment and a photosynthetic photon flux density of 800 μmol photons m<sup>-2</sup> s<sup>-1</sup> was maintained throughout the 18 h days between emergence and boot stage (days 0-60). From day 61 onwards the day length was reduced to 10 h and on day 115 (at physiological maturity) *Sorghum* seeds and shoots were harvested. Henceforth a fallow period was simulated by reducing the day/night temperatures to 5/3°C and maintaining relative humidity at 75% until the experiment was terminated on day 235.

**1.5 Irrigation regime.** Throughout the *Sorghum* lifecycle, mesocosms were weighed every 3 days using a portable laboratory balance (Navigator NVT; Ohaus, Parsippany, NJ, USA) to estimate depth-averaged soil GWC. An artificial rainwater solution (**Table S2**) was then used to approximately compensate for soil water losses via evapotranspiration, with equal volumes of solution being supplied to each mesocosm (**Fig. S4**). Irrigation water was delivered manually to the top surface of each soil column using a 1.5 L low-pressure portable sprayer (Exo Terra, Castleford, UK), with amounts measured gravimetrically to the nearest gram. Approximately every 12 d between day 0 and day 81, equal volumes of additional irrigation solution were supplied to all soil columns to produce leachate for geochemical analysis. During the simulated fallow period (days 115-235) mesocosms were weighed every 14 d and variably irrigated to maintain soil GWC at 0.38 g g<sup>-1</sup>.

**1.6 Leachate, soil extract and plant sample preparation and analysis.** Leachate was collected at six events throughout the experiment. Leachate was prepared for cation analysis by filtration of subsamples through a 0.45 μm cellulose nitrate filter (Minisart: Sartorius, Goettingen, Germany) and stabilization in a matrix of 2% (vol%) analytical-grade nitric acid. Harvested *Sorghum* root, shoot and seed tissues (collected after 235 days) were dried in a forced-air oven at 60 °C for 48 h and comminuted separately using a laboratory grinding mill (Model: A10 S2, IKA-Werke GmbH & CO. KG, Staufen, Germany). Oven-dried, powdered tissue samples were then subjected to a 45-min microwave-assisted (Model: Multiwave; Anton Paar Ltd, St Albans, UK) nitric acid-hydrogen peroxide digest (0.2 g tissue:3 mL nitric acid:3 mL MQ water:2ml hydrogen peroxide), after which extracts were prepared for cation analysis by centrifugation and filtration of the supernatant through a 0.45 μm filter. Multi-element cation analysis of all prepared leachate, plant and soil extracts was conducted at the School of Biosciences, University of Nottingham (Sutton Bonington Campus) using an iCAP Q ICP-MS (Thermo Fisher Scientific, Bremen, Germany).

**1.7 Soil sample preparation and analysis.** Soil samples were collected from all mesocosms after 235 days. Substrate was excavated from the mesocosms in five separate layers: the topsoil/amended layer (0-120 mm depth), three intermediate subsoil layers (120-240, 240-360, 360-480 mm depth) and the bottommost subsoil layer (480-500 mm depth). Each soil layer was manually comminuted into a bulk sample, homogenized, air dried at 60 °C for 48 h, and passed through a 2mm steel sieve. 100 mg of dried sample was subjected to leaching with a 1N ammonium acetate solution at pH = 8.2 in order to remove the exchangeable fraction from the solid phase (after Chapman, 1965). The resultant solid sample was dried at 60°C overnight, then heated at 600 °C for 24 hours to remove organic matter in the soil mixture. The ashed sample was then dissolved in a mixture of aqua regia (hydrochloric and nitric acid) and hydrofluoric acid as follows: 10ml aqua regia was added to Teflon beakers containing ashed sample, left to sit for 4 hours after which 1ml hydrofluoric acid was added, the beakers capped and left on a hotplate for 24 hours at 100°C. Samples were then uncapped and left to dry down on a hotplate at 90°C. Samples were raised in nitric acid and diluted to run on a Thermo Scientific iCAP Triple Quadrupole inductively coupled plasma mass spectrometer (ICP-MS) at the Yale Geochemistry Center. In order to reduce analytical error, we measured the concentrations of key elements (Ca, Mg, Ti) using an isotope dilution method (see *Supporting Information Section 1.8*).

### 1.8 Analytical requirements: isotope dilution inductively coupled plasma mass

**spectrometry (ID-ICP-MS).** In order to reduce analytical error on measurements of soil samples, we measure the concentrations of key elements (Ca, Mg, Ti) using an isotope dilution method (see also *Main Text Section 2.2*). The amount of an element in the sample,  $n_{sam}$ , is given by:

$$n_{sam} = n_{spk} \frac{R_{spk} - R_{mix} \sum_i R_{isam}}{R_{mix} - R_{sam} \sum_i R_{ispk}}, \quad (S2)$$

where  $R$  is the ratio of two isotopes, and  $\sum_i R_i$  is the sum of ratios of all isotopes to a reference isotope (e.g., 9; see also 10-11). We use an isotope spike 'cocktail', doped with isotopes of Mg, Ti, and Ca found in lower abundance in natural samples (**Fig. S5**). Isotope spikes are prepared from powders of spiked  $TiO_2$ ,  $MgCO_2$  and  $CaCO_2$ . The pure spike Mg and Ca carbonate powders are digested using HCl, and the Ti oxide using  $HNO_3+HCl+HF$ . Following the digest each spike solution is calibrated by measuring the relative concentration of Mg, Ca, and Ti isotopes on a Thermo Scientific Neptune Plus multicollector ICP-MS for ~48 hours. Estimate of the error on the spike determination are < 0.1 ‰ based on replicate analysis. Individual spike solutions are then used to make an isotope spike 'cocktail' solution containing Mg, Ca and Ti spikes. The cocktail is added to each sample during the dissolution stage of sample preparation to ensure sample-spike equilibration.

Isotope dilution allows for sample-specific calculation of element concentrations, unlike a calibration curve method whereby standards of known concentration are run to relate element intensities (in counts per second) to concentration. Isotope dilution therefore corrects for matrix effects, mass bias, and instrument drift, and thus improves both accuracy and precision of measured concentrations (**Fig. S3**; see also 12). In addition to an iCAP TQ ICP-MS, we ran standards on other ICP-MS models in order to test the data quality achieved by a variety of widely available instruments (a Perkin Elmer NexION 5000 Multi-Quadropole ICP-MS and a Thermo Scientific Element High Resolution Magnetic Sector ICP-MS).

### 1.9 Calculating weathering and carbon dioxide removal rates from leachate, soil extract and plant samples.

We employed elemental budgeting for all mesocosms in the experiment. Total amounts of Ca, Mg, and Na in all major non-solid phase pools were calculated: leachate (multiplying the concentration of cations in leachate by total volume of leachate, for each of up to six separate leachate events for each mesocosm), plant tissues (multiplying concentrations of cations in shoots, roots and seeds that underwent tissue digests by the respective mass of each tissue type collected from each mesocosm), and the soil exchangeable fraction (multiplying the concentration of cations in ammonium acetate leaches performed by the dry mass of soil at each separate depth interval for which leaches were performed),

To calculate a rate of weathering based on the additional flux of cations into non-soil pools for basalt-amended mesocosms, we subtracted from the total elemental budgets for Ca, Mg, and Na of each basalt-amended mesocosm the total elemental budget of the control mesocosm for each fertilizer scheme (NPK or manure) that in topsoil major element composition most closely matched the initial soil baseline. These were also the control mesocosms for each fertilizer scheme that yielded the smallest budget of cations in non-soil pools. Given variability in the size of elemental budgets between mesocosms of the same treatment, we report error on our calculations for cation loss as propagated standard deviations of all concentration measurements made for each treatment (NPK only, NPK + basalt, manure only, and manure + basalt). To convert from the additional flux of cations in moles to an amount of  $CO_2$  consumed, we apply a modified Steinhour formulation (as discussed in *Supporting Information Section 1.3*).

### 1.10 Calculating weathering and carbon dioxide removal rates using TiCAT.

*Main Text Section 2.1* describes the conceptual framework of the mass-balance approach used to calculate weathering rates from solid-phase samples of the soil + basalt mixture, after basalt application. Canonical approaches for estimating extent of weathering in natural systems (e.g., 13-25) define a mass transfer function for a mobile element  $j$ ,  $\tau^j$ , such that:

$$\tau_w^j = \frac{m_{flux}^j}{m_p^j} = \left( \frac{c_w^j}{c_p^j} / \frac{c_p^j}{c_p^j} \right) - 1 \quad , \quad (S3)$$

where  $m$  is mass;  $c$  is concentration;  $p$  is unweathered parent material;  $w$  is weathered material (and thus *flux* refers to mass lost from parent material during weathering); and  $i$  is a reference immobile element (14).

Here, we use titanium as this reference immobile element. Titanium is commonly used as a reference element for immobility during weathering processes. This is due to its low solubility and the chemical stability of minerals within which it is abundant (e.g., rutile, titanite). Moreover, upon initial weathering of titanium-rich minerals, Ti tends to form insoluble secondary minerals. Thus, Ti is seldom removed from the solid phase (see 15, 26-30). A similar approach could be used with other largely immobile elements such as zirconium (Zr), thorium (Th), niobium (Nb) and tantalum (Ta) (see 15, 30-34). Aluminum (Al) and Rare Earth Elements are, in many cases, also immobile (e.g., 33, 35-39). Here, we focus on Ti due to its higher abundance in the mafic minerals that constitute the best ERW feedstocks, as well as the less onerous process of dissolving Ti for laboratory analysis compared to Zr (40). It is important to note, however, that the assumption that Ti acts as an immobile element during weathering must be treated with caution, as in rare cases Ti, Zr and Th — similar to Al and REEs — act as semi-mobile elements during weathering. However, for Ti to act as a semi-mobile element, extended periods of weathering in which the soil becomes extensively depleted in cations are required. This contrasts strongly to the conditions in this experiment, or those that will prevail during ERW deployments on managed croplands (30, 34, 41-45).

We use the immobile behavior of titanium to compare the expected amount of basalt-derived cation,  $CAT_{add}$ , in a soil + basalt sample to the observed amount of cation in the sample,  $CAT_{end}$ , and calculate a fraction of basalt dissolution,  $F_D$  (see *Main Text Section 2.1*). In the canonical mass transfer framework:  $c_w^j = CAT_{end}$ ;  $c_w^i = Ti_{end}$ ;  $c_p^j = CAT_{add} + CAT_s$ ;  $c_p^i = Ti_{add} + Ti_s$ ; thus:

$$F_D = -\tau_w^j \left( \frac{CAT_{add}}{CAT_s} + 1 \right) \quad . \quad (S4)$$

Note that here,  $F_D$  of basalt specifically pertains to each cation of interest. For the purposes of estimating CDR the major cations in basalt are  $Na^+$ ,  $K^+$ ,  $Ca^{2+}$ , and  $Mg^{2+}$ . We disregard  $K^+$  here, both because it is a constituent of the NPK fertilizer added to some of our mesocosm experiments, and because it represents only a minor portion of the overall cation load.

In this study, we use an extension of this scheme to calculate  $F_D$  for each major cation: we define an additional endmember representing the fraction of basalt,  $c_d$ , that has been dissolved between the point of basalt application and the point of sampling. Thus, we resolve samples with composition  $c_{end}$  as a mixture of three components; (i) basalt feedstock ( $c_b$ ), (ii) soil baseline ( $c_s$ ), and (iii) dissolved basalt + soil ( $c_d$ ).  $c_d$  comprises the Ti concentration of the basalt endmember, but retains only those mobile elements present in the soil baseline (i.e. for all CAT,  $c_d = c_s$ ). This endmember therefore represents the loss of mobile base cations from the weathered basalt feedstock, and the buildup in the soil + basalt mixture of the immobile elements from this feedstock.

This scheme allows us to solve algebraically for all mixtures that satisfy the relationship  $c_{end} = c_s + c_b + c_d$  (where  $c_{end}$  is the sample composition). We can then calculate  $F_D$  as the ratio of the mass fraction of dissolved basalt,  $x_d$ , to the mass fraction of total basalt in the sample at the point of application,  $x_d + x_b$ , such that:

$$F_D = \frac{x_d}{x_b + x_d} \quad . \quad (S5)$$

Plotting these three endmembers defines a region in [CAT] vs [Ti] space that can be thought of as a “mixing triangle”, wherein all mixtures of soil + basalt, including those where weathering of basalt has occurred, should lie (**Fig. S7**).

The proportion of the three components that make up any soil + basalt sample within the “mixing triangle” can be solved algebraically, given a set of three linear equations that (a) describe the

bulk composition of a sample as the mass-fraction-weighted average of each component (for Ti and any CAT) and (b) enforce mass conservation. These are given as:

$$C_{end}^i = x_s c_s^i + x_b c_b^i + x_d c_d^i \quad . \quad (S6)$$

$$C_{end}^j = x_s c_s^j + x_b c_b^j + x_d c_d^j \quad . \quad (S7)$$

$$1 = x_s + x_b + x_d \quad . \quad (S8)$$

where  $i$  represents immobile and  $j$  represents cation. The  $x_{[.]}$  and  $c_{[.]}$  terms represent the mass fraction and concentration of the soil, basalt and dissolution endmembers which are labelled by  $s$ ,  $b$  and  $d$  subscripts, respectively. The  $C_{end}$  terms represent the bulk composition of the detrital element or cation in the soil-basalt mixture after dissolution. Then:

$$F_D = \frac{x_d}{x_b + x_d} \quad . \quad (S9)$$

Note that in order for these equations to have physical solutions (i.e. for each component to have a positive value), all  $C_{end}$  values must plot within the area defined as the “mixing triangle”. Several cases signify a breakdown of this scheme (**Fig. S7**):

1. Where a sample  $C_{end}$  plots above the soil – basalt mixing line, such that  $\Delta CAT < 0$  (**Fig. S7a**), this suggests that precipitation of a secondary mineral phase or phases containing cations has occurred between application of basalt and post-application sampling. This is pertinent to calculating initial CDR rates, as CO<sub>2</sub> is released by these reactions (with the exception of salt formation). In this study, we treat such samples as follows: (a) resolve  $C_{end}^j$  for the base cation in question onto the soil-basalt mixing line using  $C_{end}^i$  for that sample (such that  $c_d = 0$ ); (b) calculate the difference in [CAT] between the original  $C_{end}^j$  and the new  $C_{end}^j$  value; and (c) calculate from this cation gain a resultant CO<sub>2</sub> release per unit area (see below).
2. Where a sample  $C_{end}$  plots to the left of the “mixing triangle”, such that  $Ti_{end} < Ti_s$  (**Fig. S7b**), this indicates that the soil baseline used is unsuitable, assuming no mass transport has occurred, and as such a more suitable soil baseline is required to obtain a reliable estimate of feedstock dissolution. This is not the case for any samples in this study.
3. Where a sample  $C_{end}$  plots below the soil baseline, such that  $CAT_{end} < CAT_s$  (**Fig. S7c**), this indicates dissolution and loss of cations from the background soil. In this case it is necessary to apply the limit  $-\Delta CAT = CAT_{add}$  (i.e.,  $F_D = 1$ ).

The TiCAT approach provides a time-integrated estimate of the amount of feedstock that has dissolved between application and post-application sampling. This can be directly converted into an initial CDR rate by using a modified Steinhour formulation (*Supporting Information Section 1.3*). Assuming  $F_D$  for relevant cations CAT (Na<sup>+</sup>, Ca<sup>2+</sup>, Mg<sup>2+</sup>) in each sample (see **Fig. S8**) is representative of  $F_D$  for each mesocosm, we can calculate the total amount (mol) of each cation mobilized from applied feedstock over a given area,  $n^j$  (mol m<sup>-2</sup>):

$$n^j = F_D * A^j * \frac{10^{-3}}{M^j} \quad . \quad (S10)$$

where  $M^j$  is the molar mass of the cation, and  $A^j$  is the application rate of the cation CAT (kg m<sup>-1</sup>), calculated as:

$$A_b * \bar{c}_b^j = A^j \quad . \quad (S11)$$

where  $\bar{c}_b^j$  is the concentration of a cation in the basalt feedstock (mg kg<sup>-1</sup>), and  $A_b$  is the application rate of basalt, 5 kg m<sup>-2</sup> in this experiment.

To convert from an amount of cation dissolved,  $n^j$ , to an amount of CO<sub>2</sub> consumed during this weathering reaction, we apply the relevant Steinhour coefficient (see *Supporting Information Section 1.3*). Converting from this molar amount to a mass in kg m<sup>-2</sup> gives the total potential CO<sub>2</sub> removed by weathering of the feedstock for each cation; summed, these give total CO<sub>2</sub> removed by weathering of the feedstock in kg m<sup>-2</sup>.

In our experimental method we remove the exchangeable fraction (non-mineral-bound cations occupying exchange sites on clay mineral surfaces). However, clay and carbonate minerals are

included in the solid phase of digested soil samples, which could result in an underestimate of the extent of silicate mineral dissolution given that secondary mineral formation could reincorporate mobile cations into the solid phase following dissolution. As a result, our technique should be considered to track net cation mobility from the system, including the impact of secondary phase formation.

We use as our  $C_{\text{soil}}$  endmember a sample of bulk soil (“initial soil”) taken before the experiment was started (see **Figs. S9 and S10**). The total amount of metal cations added to each mesocosm via irrigation was negligible (see **Fig. S4 and Table S2**). Additionally, the concentration of Ti, Mg, and Na in the solid phase of manure added to half of the mesocosms was below that of the soil endmember (see *Dataset S1*), so we disregarded contributions from the manure to the  $C_{\text{end}}$  sample mixture. Even for Ca, which was enriched in manure relative to initial soil, this is a conservative approach when using the TiCAT method.

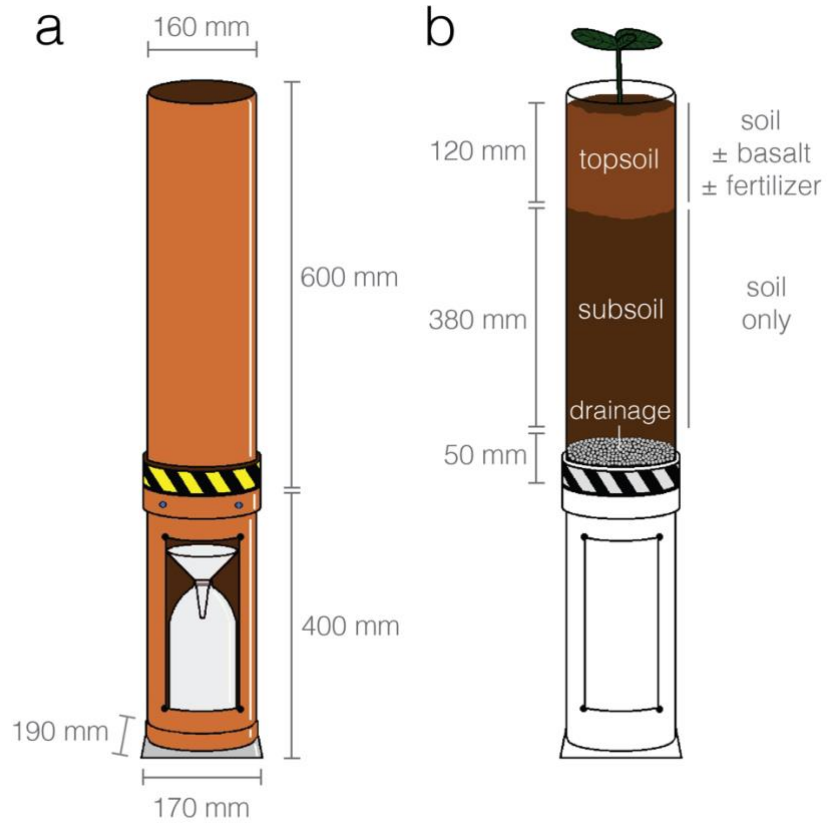


**Fig. S1.** Mesocosm design. (a) Schematic of mesocosm exterior; and (b) cutaway indicating sub- and top-soil arrangement simulating tillage regime.

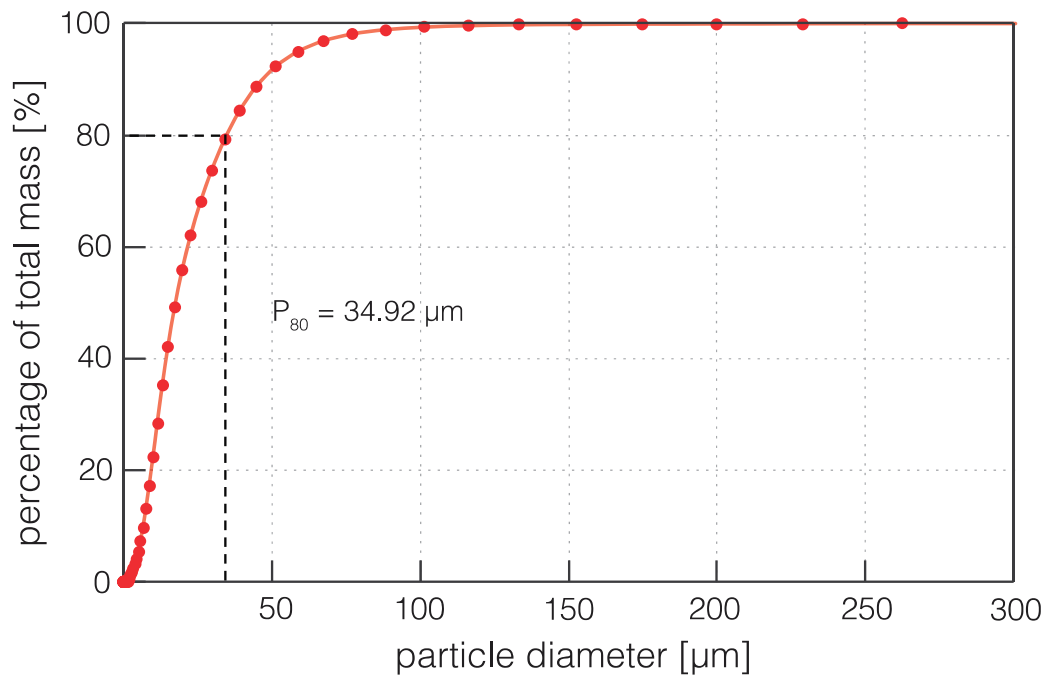


**Fig. S2.** Cumulative particle size distribution of basalt material. Determined by laser diffraction particle size distribution analysis.

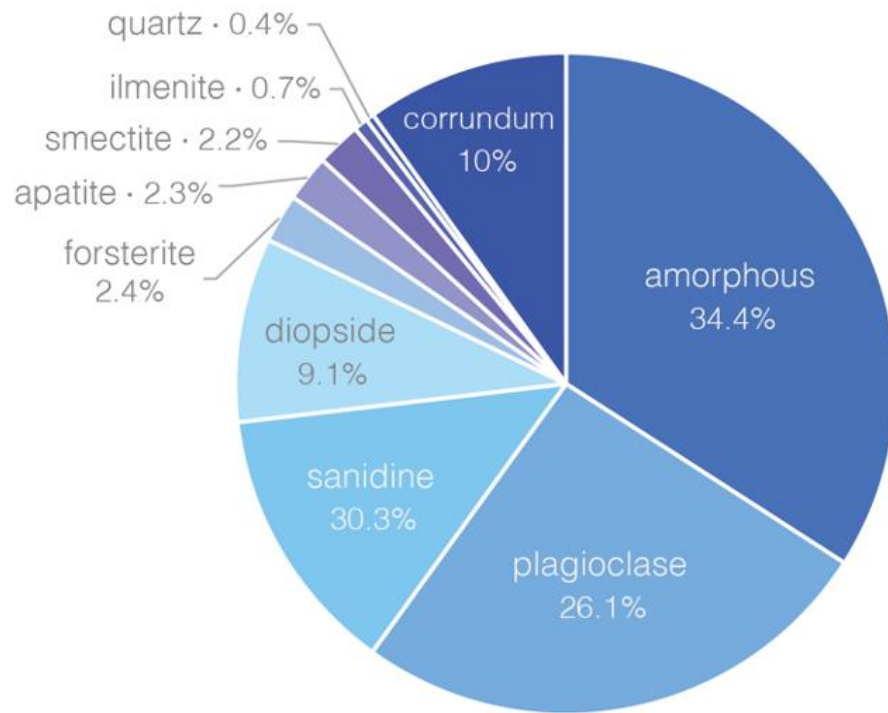


**Fig. S3.** Mineralogy of basalt material. Determined by X-Ray Diffraction analysis.

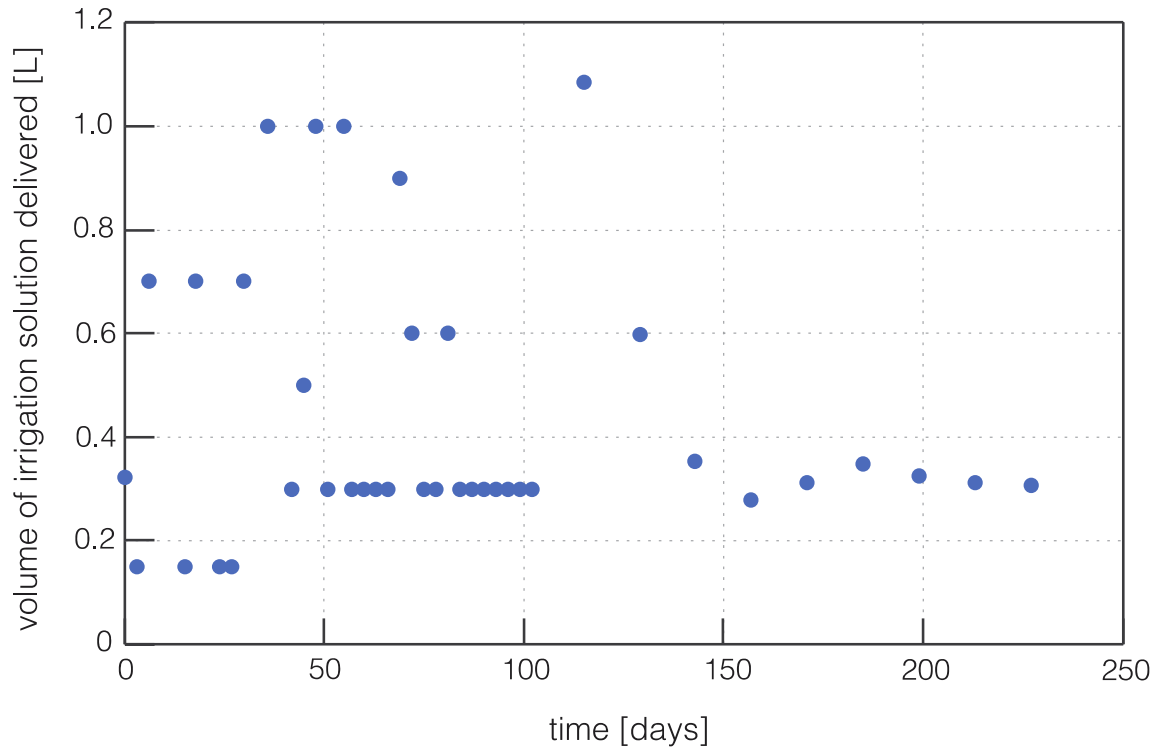


**Fig. S4.** Irrigation schedule. Volume of irrigation solution added to mesocosms.

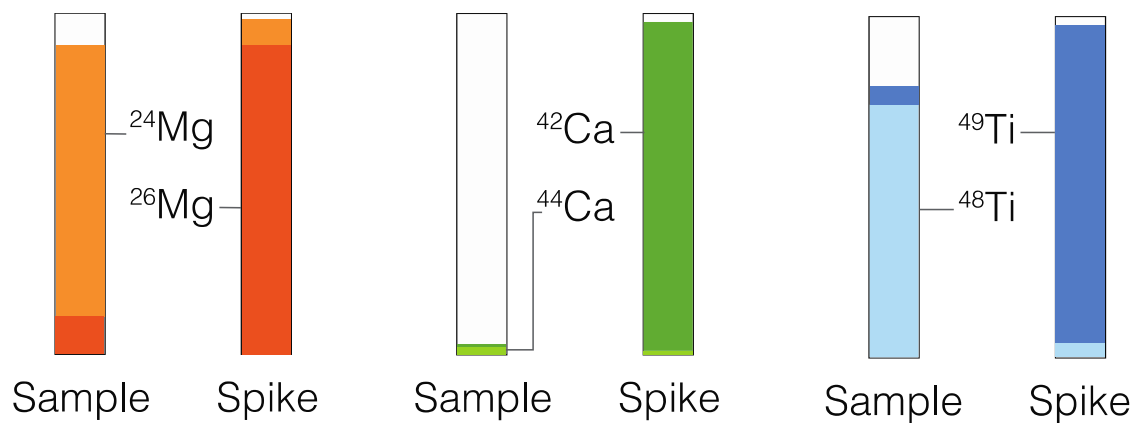


**Fig. S5.** Isotopic composition of key elements for which isotope dilution was used to reduce analytical error in this study, in natural samples (left) and the isotope spike cocktail added to the samples (right). Isotopes shown are those used in calculations.

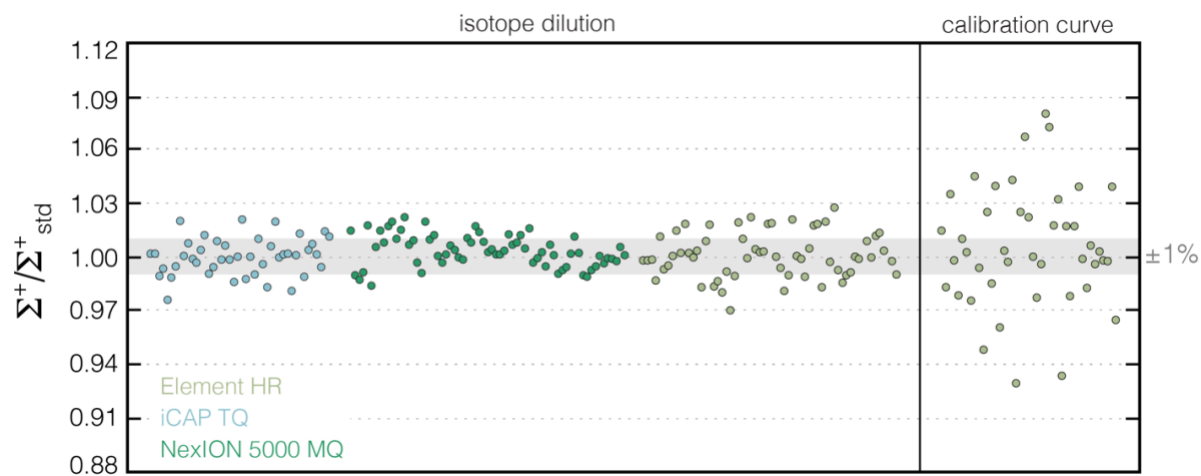


**Fig. S6.** Representative analytical error on standards (n=214) run on three different ICP-MS instruments, using a calibration curve method and our isotope dilution method. The grey shaded region represents an analytical error range of  $\pm 1\%$ . ICP-MS instruments used were two quadrupole instruments, a Thermo Scientific iCAP TQ ICP-MS and a Perkin Elmer NexION 5000 Multi-Quadropole ICP-MS; as well as a Thermo Scientific Element High Resolution Magnetic Sector ICP-MS.

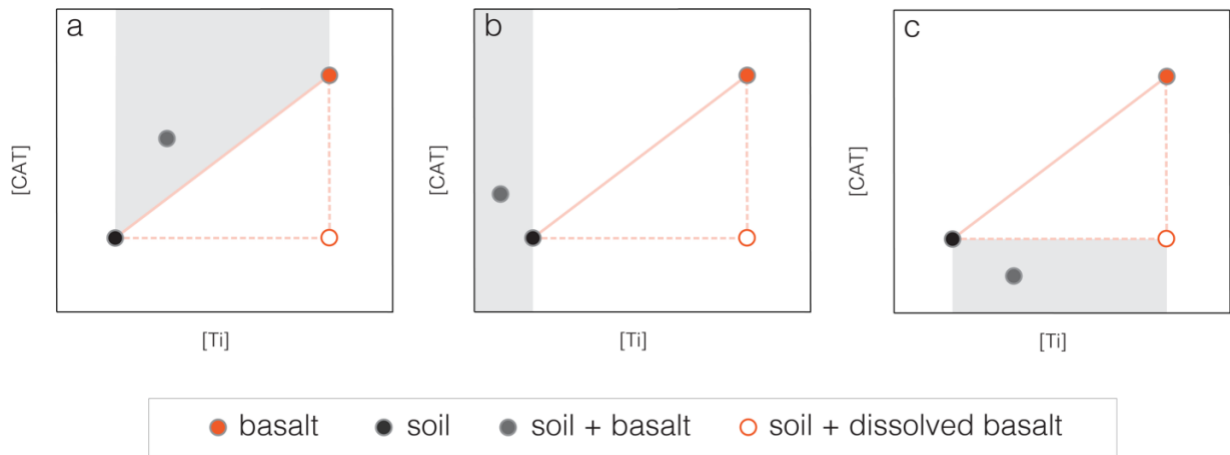


**Fig. S7.** The TiCAT conceptual framework as a three-component “mixing triangle”. The endmember soil + dissolved basalt ( $c_d$ ) has the Ti composition of the basalt endmember and the CAT composition of the soil endmember. (a-c) show cases where the composition of soil + basalt mixtures fall outside of the “mixing triangle” and therefore cannot be resolved in this framework:  $\Delta\text{CAT} < 0$ , indicating precipitation of CAT into a secondary mineral phase (a);  $\text{Ti}_{\text{end}} < \text{Ti}_{\text{soil}}$ , indicating the soil baseline value for Ti is not suitable (b);  $\text{CAT}_{\text{end}} < \text{CAT}_{\text{soil}}$ , indicating dissolution of CAT from soil (c).

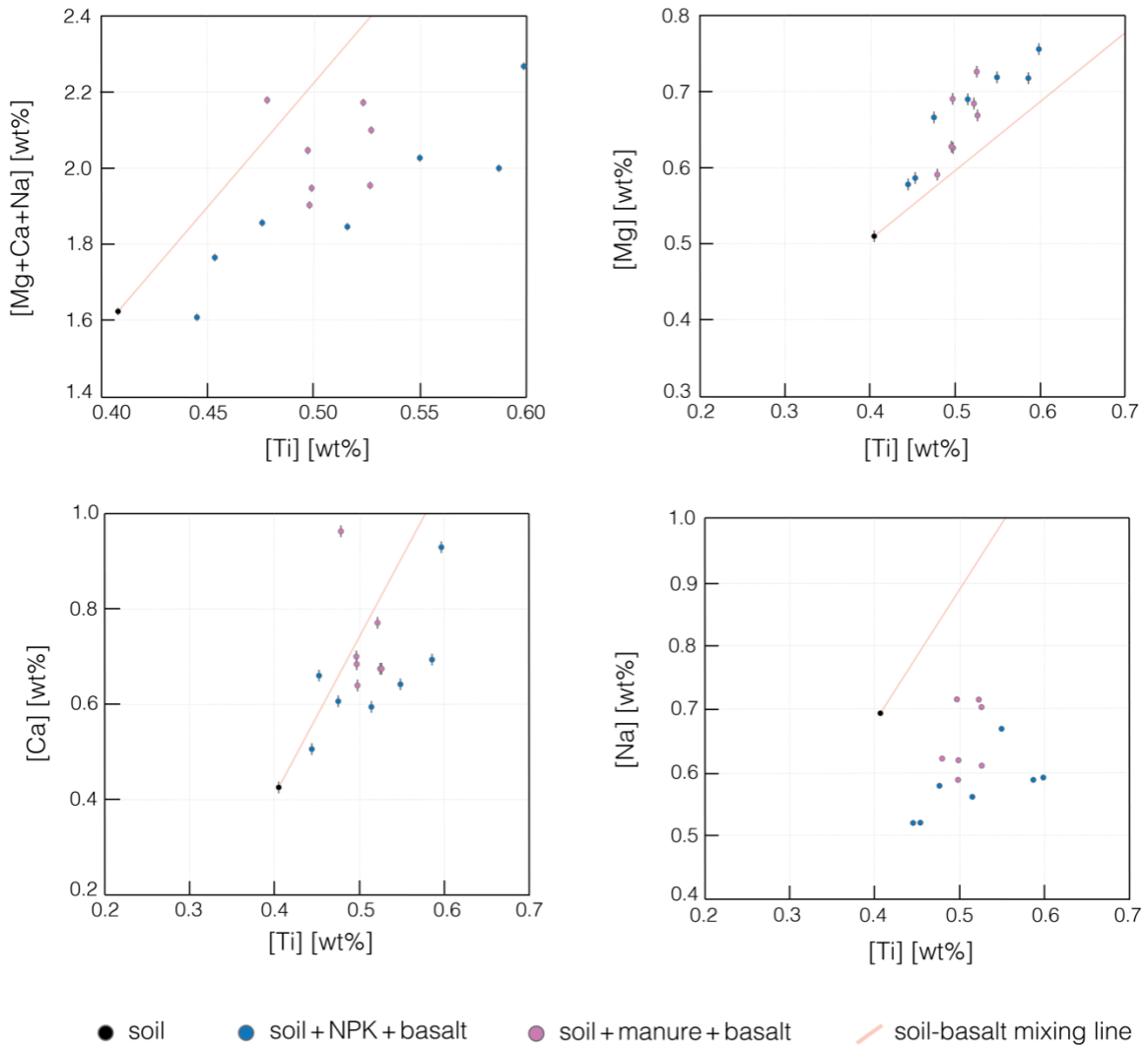


**Fig. S8.** Concentration in ashed solid samples of Mg, Ca, and Na from the “topsoil” depth interval (0-12 cm) in all basalt-amended mesocosms in this study (n=14). “Soil” is a sample of initial soil that mesocosms were filled with. Analytical error is shown (note the error bar for Na is smaller than the symbol).

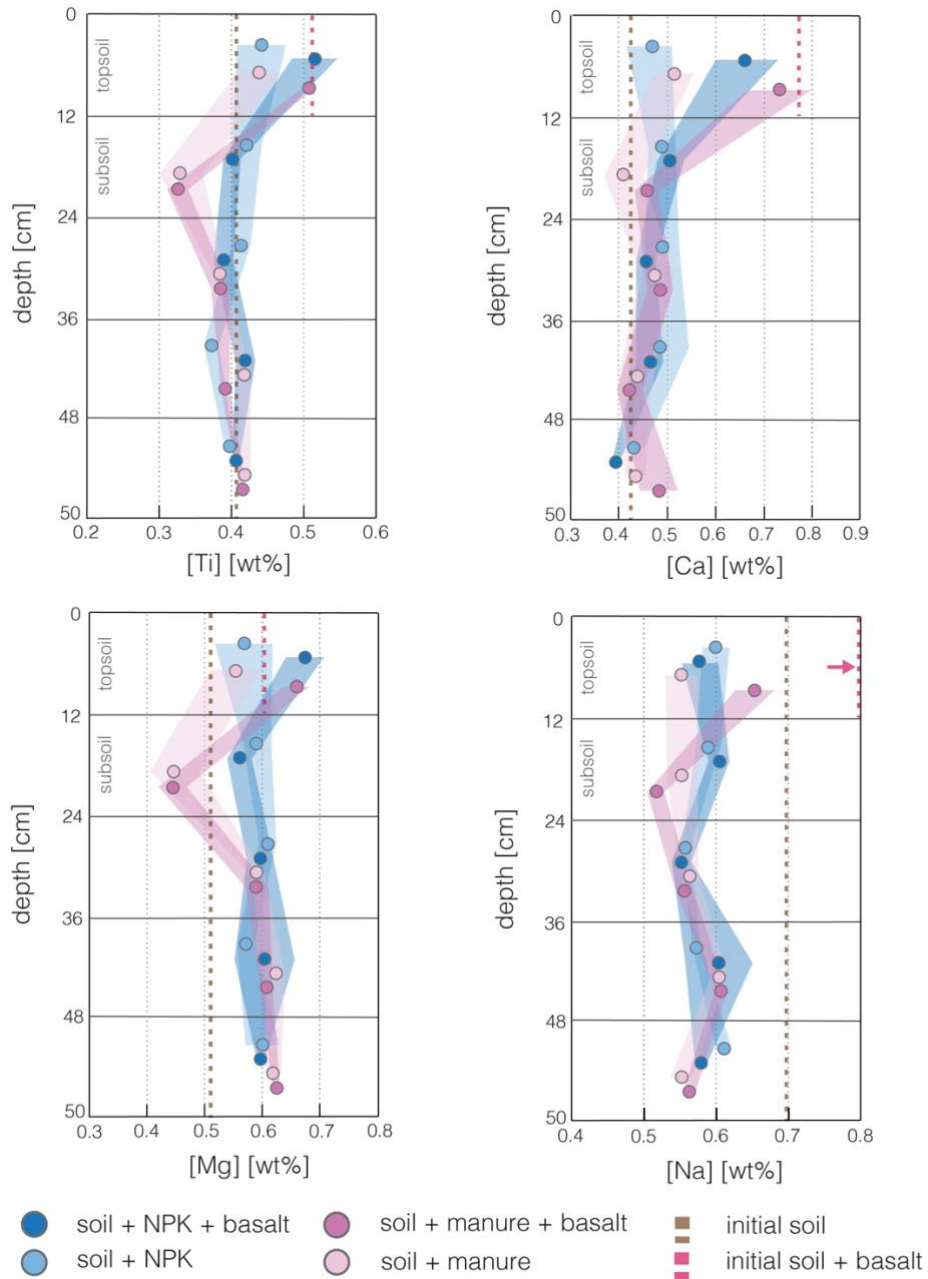


**Figure S9.** Depth profiles of concentration in ashed solid samples of Ti, Ca, Mg, and Na from mesocosms in this study. Points are averages of all columns ( $n=7$ ) for each relevant treatment, and shaded envelopes show  $\sigma$ . Samples are all homogenized across the depth interval between solid horizontal bars. Dashed brown vertical line indicates the composition of the initial soil endmember. Dashed red vertical line indicates the composition of a fully homogenized initial soil + basalt mixture in the topsoil layer, where the average additional amount of Ti is used to calculate average basalt addition rate in samples.

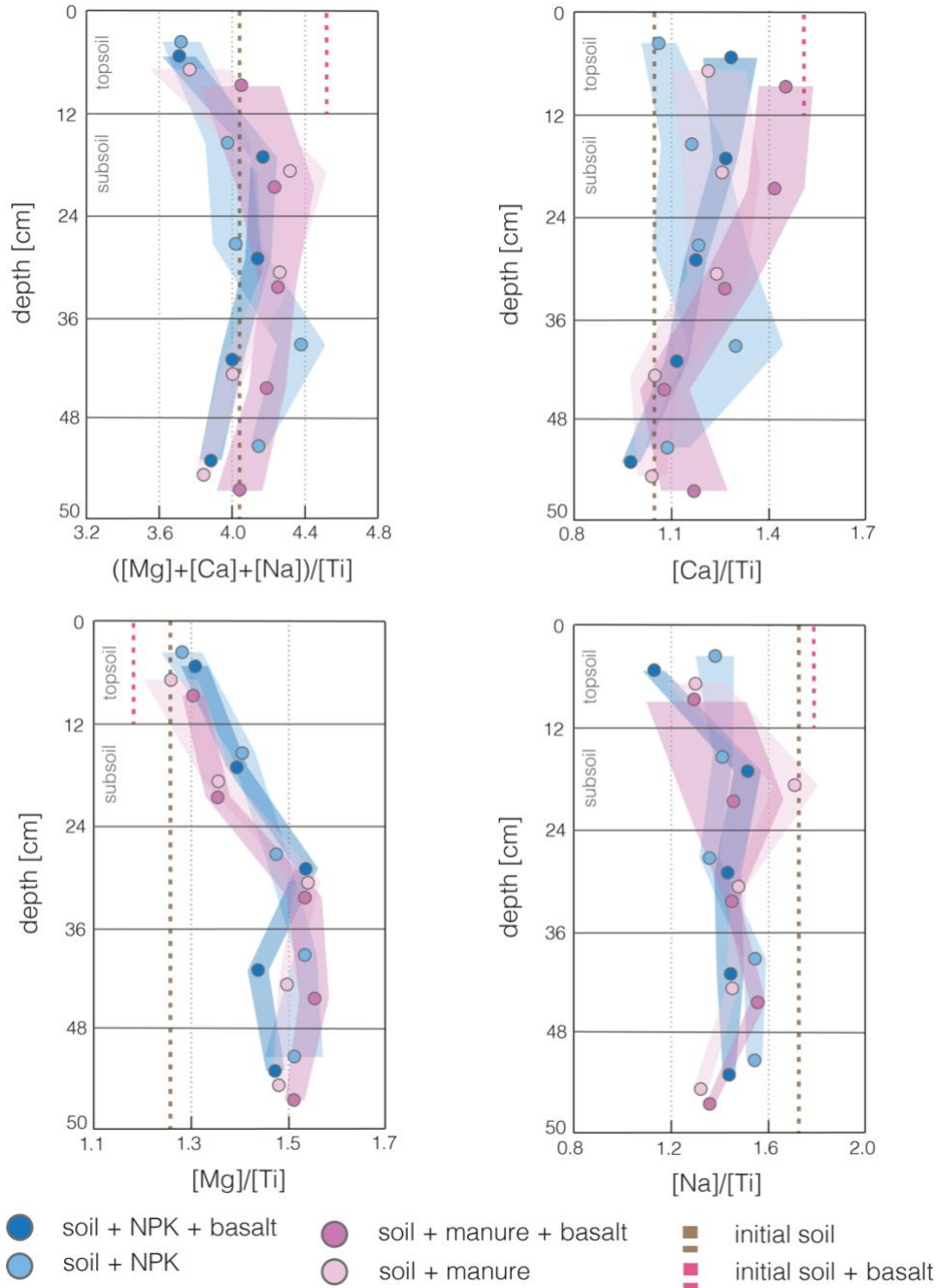


**Figure S10.** Depth profiles of ratios in concentration in ashed solid samples of  $(\text{Ca}+\text{Mg}+\text{Na})/\text{Ti}$ ,  $\text{Ca}/\text{Ti}$ ,  $\text{Mg}/\text{Ti}$ , and  $\text{Na}/\text{Ti}$  from mesocosms in this study. Points are averages of all columns ( $n=7$ ) for each relevant treatment, and shaded envelopes show  $2\sigma$ . Samples are all homogenized across the depth interval between solid horizontal bars. Dashed brown vertical line indicates the composition of the initial soil endmember. Dashed red vertical line indicates the composition of a fully homogenized initial soil + basalt mixture in the topsoil layer, where the average additional amount of Ti is used to calculate average basalt addition rate in samples.

**Table S1.** Chemical composition (major oxides) of basalt feedstock used, Columbia River Basalt, Prineville Chemical Type Unit. Bulk rock total digest (HF+HNO<sub>3</sub>+HCl), measured on Element HR-ICP-MS. See also Kelland et al., 2020, and Lewis et al., 2021, for further chemical and textural information about the feedstock used.

<b>Oxide</b>	<b>Concentration (wt%)</b>
<b>CaO</b>	5.26
<b>MgO</b>	2.37
<b>Na<sub>2</sub>O</b>	3.79
<b>K<sub>2</sub>O</b>	3.02

**Table S2.** Chemical composition of artificial rainwater irrigation solution.

<b>Salt</b>	<b>Solution concentration (mg L<sup>-1</sup>)</b>
<b>NaNO<sub>3</sub></b>	0.000135
<b>NaCl</b>	0.004790
<b>CaCl<sub>2</sub>.2H<sub>2</sub>O</b>	0.001100
<b>K<sub>2</sub>SO<sub>4</sub></b>	0.000450
<b>MgSO<sub>4</sub>.7H<sub>2</sub>O</b>	0.002050
<b>(NH<sub>4</sub>)<sub>2</sub>SO<sub>4</sub></b>	0.002270

**Dataset S1 (separate file).** Dataset containing processed ICP-MS concentration values for leachate, plant (shoots, roots, and seeds), soil exchangeable fraction, and soil solid phase.

**Software S1 (separate file).** MATLAB code TiCAT\_X.m with requisite .xlsx sheets.

## SI References

1. A. L. Lewis, B. Sarkar, P. Wade, S. J. Kemp, M. E. Hodson, L. L. Taylor, K. L. Yeong, K. Davies, P. N. Nelson, M. I. Bird, I. B. Kantola, M. D. Masters, E. DeLucia, J. R. Leake, S. A. Banwart, D. J. Beerling, Effects of mineralogy, chemistry and physical properties of basalts on carbon capture potential and plant-nutrient element release via enhanced weathering. *Appl Geochem.* 132, 105023 (2021).
2. H. H. Steinour, Some effects of carbon dioxide on mortars and concrete-discussion. *J. Am. Concrete I* 30, 905 (1959).
3. M. Fernández Bertos, S. J. R. Simons, C. D. Hills, P. J. Carey, A review of accelerated carbonation technology in the treatment of cement-based materials and sequestration of CO<sub>2</sub>. *J. Hazard Mater* 112, 193–205 (2004).
4. P. J. Gunning, C. D. Hills, P. J. Carey, Accelerated carbonation treatment of industrial wastes. *Waste Manage.* 30, 1081–1090 (2010).
5. P. Renforth, The negative emission potential of alkaline materials. *Nat. Commun.* 10, 1401 (2019).
6. L. A. Bullock, R. H. James, J. Matter, P. Renforth, D. A. H. Teagle, Global Carbon Dioxide Removal Potential of Waste Materials From Metal and Diamond Mining. *Frontiers Clim* 3, 694175 (2021).
7. T. Rinder, C. von Hagke, The influence of particle size on the potential of enhanced basalt weathering for carbon dioxide removal - Insights from a regional assessment. *J Clean Prod* 315, 128178 (2021).
8. P. Renforth, The potential of enhanced weathering in the UK. *Int J Greenh Gas Con* 10, 229–243 (2012).
9. M. G. Inghram, Stable isotope dilution as an analytical tool. *Ann Rev Nucl Sci* 4:1, 81-92 (1954).
10. E. H. Evans, R. Clough, “Isotope dilution analysis” in Encyclopedia of Analytical Science 2<sup>nd</sup> ed., P. Worsfold, A. Townshend, C. Poole, Eds. (Elsevier, 2005), pp. 545-553.
11. A. Stracke, E. E. Scherer, B. C. Reynolds, Application of isotope dilution in geochemistry, *Treatise on Geochemistry 2<sup>nd</sup> ed.* 71–86 (2014).
12. M. Willbold, K. P. Jochum, Multi-Element Isotope Dilution Sector Field ICP-MS: A Precise Technique for the Analysis of Geological Materials and its Application to Geological Reference Materials. *Geostand Geoanal Res* 29, 63–82 (2005).
13. G. H. Brimhall, W. E. Dietrich, Constitutive mass balance relations between chemical composition, volume, density, porosity, and strain in metasomatic hydrochemical systems: Results on weathering and pedogenesis. *Geochim Cosmochim Ac* 51, 567–587 (1987).
14. O. A. Chadwick, G. H. Brimhall, D. M. Hendricks, From a black to a gray box — a mass balance interpretation of pedogenesis. *Geomorphology* 3, 369–390 (1990).
15. G. H. Brimhall, C. J. Lewis, C. Ford, J. Bratt, G. Taylor, O. Warin, Quantitative geochemical approach to pedogenesis: importance of parent material reduction, volumetric expansion, and eolian influx in lateritization. *Geoderma* 51, 51–91 (1991).
16. O. A. Chadwick, L. A. Derry, P. M. Vitousek, B. J. Huebert, L. O. Hedin, Changing sources of nutrients during four million years of ecosystem development. *Nature* 397, 491–497 (1999).
17. A. C. Kurtz, L. A. Derry, O. A. Chadwick, M. J. Alfano, Refractory element mobility in volcanic soils. *Geology* 28, 683–686 (2000).

18. A. F. White, T. D. Bullen, M. S. Schulz, A. E. Blum, T. G. Huntington, N. E. Peters, Differential rates of feldspar weathering in granitic regoliths. *Geochim Cosmochim Acta* **65**, 847–869 (2001).
19. S. P. Anderson, W. E. Dietrich, G. H. Brimhall, Weathering profiles, mass-balance analysis, and rates of solute loss: Linkages between weathering and erosion in a small, steep catchment. *Gsa Bulletin* **114**, 1143–1158 (2002).
20. C. S. Riebe, J. W. Kirchner, R. C. Finkel, Long-term rates of chemical weathering and physical erosion from cosmogenic nuclides and geochemical mass balance. *Geochim Cosmochim Acta* **67**, 4411–4427 (2003).
21. N. J. Tabor, I. P. Montañez, R. Zierenberg, B. S. Currie, Mineralogical and geochemical evolution of a basalt-hosted fossil soil (Late Triassic, Ischigualasto Formation, northwest Argentina): Potential for paleoenvironmental reconstruction. *GSA Bulletin* **116**, 1280–1293 (2004).
22. N. D. Sheldon, N. J. Tabor, Quantitative paleoenvironmental and paleoclimatic reconstruction using paleosols. *Earth-sci Rev* **95**, 1–52 (2009).
23. S. L. Brantley, M. Lebedeva, Learning to Read the Chemistry of Regolith to Understand the Critical Zone. *Annu Rev Earth Pl Sc* **39**, 387–416 (2011).
24. B. A. Fisher, A. K. Rendahl, A. K. Aufdenkampe, K. Yoo, Quantifying weathering on variable rocks, an extension of geochemical mass balance: Critical zone and landscape evolution. *Earth Surf. Process. Landforms* **42**, 2457–2468 (2017).
25. A. G. Lipp, O. Shorttle, E. A. Sperling, J. J. Brocks, D. B. Cole, P. W. Crockford, L. D. Mouro, K. Dewing, S. Q. Dornbos, J. F. Emmings, U. C. Farrell, A. Jarrett, B. W. Johnson, P. Kabanov, C. B. Keller, M. Kunzmann, A. J. Miller, N. T. Mills, B. O'Connell, S. E. Peters, N. J. Planavsky, S. R. Ritzer, S. D. Schoepfer, P. R. Wilby, J. Yang, The composition and weathering of the continents over geologic time. *Geochem Perspectives Lett* **21–26** (2021).
26. S. K. Monro, F. C. Loughnan, M. C. Walker, “The Ayrshire bauxitic clay: An allochthonous deposit?” in R. C. L. Wilson, Ed., *Residual deposits: Geological Society (London) Special Publication 11*, 47–58 (1983)
27. J. J. Middelburg, C. H. van der Weijden, J. R. W. Woittiez, Chemical processes affecting the mobility of major, minor and trace elements during weathering of granitic rocks. *Chem Geol* **68**, 253–273 (1988).
28. D. B. Tilley, R. A. Eggleton, Titanite Low-Temperature Alteration and Ti Mobility. *Clay Miner* **53**, 100–107 (2005).
29. T. Taboada, A. M. Cortizas, C. García, E. García-Rodeja, Particle-size fractionation of titanium and zirconium during weathering and pedogenesis of granitic rocks in NW Spain. *Geoderma* **131**, 218–236 (2006).
30. X. Du, A. W. Rate, M. A. M. Gee, Redistribution and mobilization of titanium, zirconium and thorium in an intensely weathered lateritic profile in Western Australia. *Chem Geol* **330**, 101–115 (2012).
31. D. Langmuir, J. S. Herman, The mobility of thorium in natural waters at low temperatures. *Geochim Cosmochim Acta* **44**, 1753–1766 (1980).
32. J.-J. Braun, M. Pagel, A. Herbilln, C. Rosin, Mobilization and redistribution of REEs and thorium in a syenitic lateritic profile: A mass balance study. *Geochim Cosmochim Acta* **57**, 4419–4434 (1993).
33. M. G. Little, C.-T. A. Lee, Sequential extraction of labile elements and chemical characterization of a basaltic soil from Mt. Meru, Tanzania. *J Afr Earth Sci* **57**, 444–454 (2010).
34. K. Jiang, H.-W. Qi, R.-Z. Hu, Element mobilization and redistribution under extreme tropical weathering of basalts from the Hainan Island, South China. *J Asian Earth Sci* **158**, 80–102 (2018).
35. H. W. Nesbitt, Mobility and fractionation of rare earth elements during weathering of a granodiorite. *Nature* **279**, 206–210 (1979).
36. M. A. Gouveia, M. I. Prudêncio, M. O. Figueiredo, L. C. J. Pereira, J. C. Waerenborgh, I. Morgado, T. Pena, A. Lopes, Behavior of REE and other trace and major elements during weathering of granitic rocks, Évora, Portugal. *Chem Geol* **107**, 293–296 (1993).

37. B. Boulangé, F. Colin, Rare earth element mobility during conversion of nepheline syenite into lateritic bauxite at Passa Quatro, Minas Gerais, Brazil. *Appl Geochem* 9, 701–711 (1994).
38. B. Öhlander, M. Land, J. Ingri, A. Widerlund, Mobility of rare earth elements during weathering of till in northern Sweden. *Appl Geochem* 11, 93–99 (1996).
39. E. Tertre, A. Hofmann, G. Berger, Rare earth element sorption by basaltic rock: Experimental data and modeling results using the “Generalised Composite approach.” *Geochim Cosmochim Acta* 72, 1043–1056 (2008).
40. J. C. Jain, C. R. Neal, J. M. Hanchar, Problems Associated with the Determination of Rare Earth Elements of a “Gem” Quality Zircon by Inductively Coupled Plasma-Mass Spectrometry. *Geostandard Newslett* 25, 229–237 (2001).
41. A. J. Melfi, F. Subies, D. Nahon, M. L. L. Formoso, Zirconium mobility in bauxites of Southern Brazil. *J S Am Earth Sci* 9, 161–170 (1996).
42. S. Cornu, Y. Lucas, E. Lebon, J. P. Ambrosi, F. Luizão, J. Rouiller, M. Bonnay, C. Neal, Evidence of titanium mobility in soil profiles, Manaus, central Amazonia. *Geoderma* 91, 281–295 (1999).
43. I. G. Hill, R. H. Worden, I. G. Meighan, Yttrium: The immobility-mobility transition during basaltic weathering. *Geology* 28, 923–926 (2000).
44. M. E. Hodson, Experimental evidence for mobility of Zr and other trace elements in soils. *Geochim Cosmochim Acta* 66, 819–828 (2002).
45. A. J. Bednar, D. B. Gent, J. R. Gilmore, T. C. Sturgis, S. L. Larson, Mechanisms of Thorium Migration in a Semiarid Soil. *J Environ Qual* 33, 2070–2077 (2004).